HOKKAIDO UNIVERSITY

Title	Bidirectional Loading Response of Square-HSS Columns and Panel Zones Measured in Shake-Table Tests of a 10-Story Steel Building
Author(s)	Li, Jionghui; Jin, Jialiang; Yan, Tianhao et al.
Citation	Journal of structural engineering, 151(5), 04025050 https://doi.org/10.1061/JSENDH.STENG-13984
Issue Date	2025-05
Doc URL	https://hdl.handle.net/2115/94898
Rights	This material may be downloaded for personal use only. Any other use requires prior permission of ASCE. This material may be found at https://doi.org/10.1061/JSENDH.STENG-13984.
Type	journal article
File Information	20241016_revised manuscript.pdf

Hokkaido University Collection of Scholarly and Academic Papers : HUSCAP

Bidirectional Loading Response of Square-HSS Columns and Panel Zones Measured in Shake-Table Tests of a 10-Story Steel Building

Jionghui Li[1]; Jialiang Jin[2]; Tianhao Yan[3]; Jun Fujiwara[4]; Koichi Kajiwara[5]; Akiko Kishida[6]; Ryota Nishi[7]; Takuya Nagae[8]; Tatsuya Asai[9]; and Taichiro Okazaki[10], M. ASCE

Abstract: A series of shake-table tests on a nearly-full-scale, 10-story steel moment-resisting frame with buckling-restrained braces (BRBs) were conducted at the E-Defense shake-table facility in February 2023. The specimen was subjected to a 3D strong motion recorded from the 1995 Kobe earthquake, scaled from 25% to 100%. Yielding of the interior columns and column panel zones was expected from the relative proportions of the columns and beams. At one of the interior grid points, responses of such interior column, panel zones, BRBs and connecting beams were instrumented to understand the interaction between the members under real, dynamic loading environment. During the 100% JMA Kobe motion, the specimen yielded in the 1st to 8th stories developing maximum story drift ratios of 0.020 rad and 0.017 rad in the two orthogonal directions. As expected, the column and panel zones in the interior grid point yielded under biaxial forces, while the connecting beams remained elastic. Methods to estimate panel-zone shear force and strength were devised to match the measured responses. A 2D numerical model of BRB-to-beam-to-column joints was calibrated to match the measured column inflection points and panel-zone deformation. Time history analysis of the frame using the calibrated model reproduced the experimental results with acceptable consistency.

Keywords: Shake-table test; Steel moment-resisting frame; Column; Panel zone; Numerical simulation

[1] Graduate student, Graduate School of Engineering, Hokkaido University, Sapporo, Hokkaido 060-8628, Japan (corresponding author). E-mail: jionghui.li.f9@elms.hokudai.ac.jp

[2] Graduate student, Graduate School of Environmental Studies, Nagoya University, Aichi, Nagoya 464-8601, Japan.

E-mail: j1822238004@gmail.com
[3] Graduate student, Graduate School of Environmental Studies, Nagoya University, Aichi, Nagoya 464-8601, Japan. E-mail: yan.tianhao.d8@s.mail.nagoya-u.ac.jp
[4] Senior Research Fellow, National Research Institute for Earth Science and Disaster Resilience (NIED), Miki, Hyogo 673-0515, Japan. E-mail: j.fujiwara@bosai.go.jp
[5] Project Director, National Research Institute for Earth Science and Disaster Resilience (NIED), Miki, Hyogo 673-0515, Japan. E-mail: kaji@bosai.go.jp
[6] Senior Research Fellow, National Research Institute for Earth Science and Disaster Resilience (NIED), Miki, Hyogo 673-0515, Japan. E-mail: akiko_kishida@bosai.go.jp
[7] Technical Staff, National Research Institute for Earth Science and Disaster Resilience (NIED), Miki, Hyogo 673-0515, Japan. E-mail: nishi.r@bosai.go.jp
[8] Associate professor, Disaster Mitigation Research Center Division, Nagoya University, Nagoya 464-8601, Japan. E-mail: nagae.takuya.h9@f.mail.nagoya-u.ac.jp
[9] Associate Professor, Institute of Industrial Science, The University of Tokyo, Tokyo, 153-8505, Japan. E-mail: asait@iis.u-tokyo.ac.jp
[10] Professor, Faculty of Engineering, Hokkaido University, Sapporo, Hokkaido 060-8628, Japan. E-mail: tokazaki@eng.hokudai.ac.jp

Introduction

This paper studies the seismic response of column panel zones in steel moment-resisting frames (MRFs) comprising square hollow-structural-section (HSS) columns and I-section beams. The seismic response of such column panel zones can be complicated by axial forces, biaxial loading, yielding of the surrounding beams and columns, and presence of composite reinforced-concrete slab among other factors. The complication is a real issue in Japan where steel buildings generally adopt moment-resisting connections at all beam-to-column joints, and therefore, bidirectional loading effects are unavoidable. (Configuration of a typical Japanese MRF will be described in the next section). When these buildings adopt buckling-restrained braces (BRBs), bracing connections framing to the moment-resisting beam-to-column connections cause additional complications.

Design of MRFs has allowed yielding in column panel zones due to their favorable energy dissipation and plastic deformation capacity (Gupta and Krawinkler 1999; Kim and Engelhardt 2002; AIJ 2021). The behavior of column panel zones is generally dominated by shear forces but their shear strength reduces in the presence of force components other than shear. Interaction

between column axial force and panel shear strength in a single plane (unidirectional loading) has been considered in design codes worldwide, for example, by AIJ (2021) and AISC (2016c). In Japan, where MRFs tend to comprise square-HSS columns, the panel zone response under bidirectional loading has been studied experimentally and theoretically. Wang et al. (2018) tested beam-and-column subassemblages under cyclic unidirectional and bidirectional loadings with no axial force, where the specimens were proportioned to yield in the panel zone. They found that bidirectional loading tended to reduce panel zone strength compared to unidirectional loading and tended to promote fracture at the corner of the panel-to-diaphragm welds. Arakida et al. (2019) conducted cyclic loading tests on isolated column panels bounded by through-diaphragm plates to study the effect of loading direction, axial force, and beam height-to-column depth ratio on panel zone response. Based on plane-stress analysis and Mises yield criterion, they deduced interaction equations between axial force and shear force in arbitrary loading direction. The equations are relevant to this paper and are summarized in the Appendix. Suita et al. (2008) reported panel zone response measured in shake-table tests on a 2-by-1 bay, 4-story steel MRF building with 175 and 150-mm thick composite slab. The building specimen yielded first in the panel zones and ultimately collapsed due to local buckling in the first story columns. The measured shear force in the panel zone was found to exceed the plastic strength based on design equations. Yamada et al. (2009) explained that the panel-zone shear force measured by Suita et al. (2008) closely matched the force couple placed at the centers of slab and beam bottom flange, while the plastic strength per design equations placed force couple at the centers of through-diaphragm plates. Therefore, Yamada et al. (2009) suggested decomposing the bending moment into a force couple acting at the centers of slab and beam bottom flange to deduce panel-zone shear force. Kishiki et al. (2010) suggested an alternative method to decompose the beam moment into a force couple at the centers

of slab and steel beam plus bending moment in steel beam, and further replace the forces in the steel beam by concentrated forces at beam upper and lower flanges.

Buckling-restrained braces connecting to beam-to-column joints can complicate the force transfer mechanism at the joints and thereby create another challenge in predicting panel zone behavior. Kishiki et al. (2007) conducted cyclic loading tests on BRB-braced portal frames where the gusset plates were welded to I-section beams and square-HSS columns with no edge stiffener. They found that close to the gusset-to-column interface, normal stress distributed linearly, while shear stress distributed nearly uniformly. Kasai et al. (2015) tested subassemblages that closely represented the loading environment of a BRB-braced MRF. The BRB gusset plate welded to beam and column was stiffened at the edges. They found that close to the beam-end section and gusset-to-column interface, the measured principal strain distributed linearly. The findings by Kishiki et al. (2007) and Kasai et al. (2015) imply that the stresses at the gusset plate interface may be estimated adequately by the plane-section assumption.

Gupta and Krawinkler (1999) proposed modeling column panel zones with rigid bars connected in a parallelogram shape through hinges and an elasto-plastic rotational spring with a trilinear backbone curve. Skiadopoulos et al. (2021) improved the stiffness and yielding strength of the rotational spring to achieve more accurate predictions over a wider range of column panel zones. In order to account for reinforced-concrete floor slab composited with steel beam, Elkady and Lignos (2014) proposed computing the yield moment of the rotational spring based on the center-to-center distance between beam lower flange and floor slab, which is the same method proposed by Yamada et al. (2009) mentioned above. El Jisr et al. (2022) proposed to explicitly model the floor slab by axial springs at slab center connected to column surface. To the knowledge of the authors, there is no established scheme to model panel zones that are stiffened by a bracing

connection. Hsiao et al. (2013) modeled brace-beam-column joints with three rigid bars connected rigidly and neglected panel-zone deformation. Mojiri et al. (2021) improved the joint model proposed by Hsiao et al. (2013) by adding a rotational spring between the gusset plate and BRB to represent the flexural stiffness of the gusset plate. Kaneko et al. (2008) and Kishiki et al. (2008) proposed adding a diagonal truss element with calibrated stiffness between the beam and column to simulate the stiffening effect due to gusset plate.

In February 2023, a 3-by-3 bay, nearly-full-scale, 10-story building specimen was tested at the E-Defense shake-table facility in Japan. The specimen had a wide variety of non-structural elements installed such as glazed curtain walls, ceilings, and ventilation ducts. This paper presents the structural responses of the specimen, focusing on the measured response of an interior column and its surrounding members. The interior columns and their panel zones were expected to yield under combined compression, biaxial shear and bending, while the connecting beams were expected to remain elastic. Indeed, the column and panel zones yielded under complicated multi-axial loading. The measured responses are reported and compared against theoretical predictions. A method to deduce panel-zone shear force considering the slab and BRB gusset plate is described, and a method to estimate force interaction in panel zones is discussed. Finally, computed responses of a structural model with proposed modeling schemes are reported. The broader scope and preliminary results of the test are reported by Fujiwara et al. (2024) and Li et al. (2024). The performance of non-structural elements will be reported in future publications.

Shake-Table Test Plan

Specimen

Fig.1 shows a photograph and Fig. 2 shows elevations and floor layout of the 10-story specimen. The specimen was an MRF with a floor layout of 12×8 m in longitudinal (*Y*) and transverse (*X*) directions and floor-to-floor story heights between 2.5 and 2.8 m. The specimen was designed and detailed according to the Building Standard Law of Japan (MLIT 2020). The steel frame comprised BCR295 (specified minimum yield strength, F_y = 295 N/mm^2) formed-from-round cold-formed, square-HSS columns with depths of either 250 or 350 mm, and JIS grade SN400B (F_y = 235 N/mm^2) I-section steel beams with depths between 244 and 350 mm. Tables 1 and 2 list the column and beam sections. As shown in Fig. 2(b), BRBs were installed in the two interior frames (Frames B and C) through the 1st to 7th stories in the *Y*-direction only. Fig. 3 shows details of a BRB and the dimensions of the LY225 (F_y = 205 N/mm^2) steel core, where L_t is the total length, and L_c and W_c are the length and width of the yielding segment. Table 3 summarizes the mechanical properties of the columns, beams, and BRB steel cores measured from tensile coupon tests.

To balance the story stiffnesses between the *X*- and *Y*-directions, the former with short beam spans and the latter with BRBs, smaller beams were chosen for the interior frames in the *Y*-direction, and smaller columns were selected for the interior compared to for the perimeter. As a result, the specimen had weak column-strong beam proportions at the grid points along frame lines B and C. However, it is emphasized that the Japanese design code (MLIT 2020) allows yielding in the column and/or panel zones so long as the strong column-weak beam (and weak panel) proportion is satisfied as sum over the floor, i.e., the sum of plastic moments of all columns above and below the floor is greater than the sum of the smaller of 1.5 times plastic moments of the left and right beams or 1.3 times plastic strength of the panel zone at each joint at the floor (MLIT 2020). This requirement was satisfied at every floor of the specimen. The columns at these grid

points were expected to develop considerable axial forces due to the BRBs placed in the *Y*-direction and the short beam span in the *X*-direction. Fig. 4 shows a beam-to-column connection at grid point 2C of the 3rd floor. The beam-to-column connection adopted a welded flange-welded web detail with no weld-access hole at the beam flanges, which is the most common detail in Japan. The deeper *X*-direction beams had the flanges welded to protruding, through-diaphragm plates. The shallower *Y*-direction beam had the top flange match height with the upper through-diaphragm plate but the bottom flange welded directly to the column. The column was stiffened with an interior diaphragm plate at the bottom flange of this *Y*-direction beam. In the *Y*-direction, a BRB gusset plate was connected to the beam and column using all-around fillet welds and was stiffened at the vertical and horizontal edges. Both the column and beam were stiffened at the gusset edge stiffeners. A 110-mm thick, reinforced-concrete slab was cast on flat-on-top metal deck using normal weight concrete with a measured compressive strength of 39 N/mm^2. Shear studs of ϕ16×80 mm were placed at 200-mm intervals to achieve fully-composite action per Japanese design guides (AIJ 2023).

Excitation Plan

The specimen was subjected to the 3D excitations listed in Table 4. The primary excitations were the Japan Meteorological Agency (JMA) Kobe record from the 1995 Kobe earthquake, scaled from 25% to 100%. The North-South component of the record was assigned to the *Y*-direction, the East-West component to the *X*-direction, and the Up-Down component to the *Z*-direction. Fig. 5 shows the pseudo-acceleration-response spectrums of the target and realized 100% *Y*- and *X*-motions. The realized motions agreed with the target near the measured fundamental vibration periods (mentioned later in Fig. 10) but were somewhat larger than the target over periods shorter than 0.5 s. Between the JMA Kobe motions, the specimen was subjected to a 3D white-noise

171 excitation with a duration of 140 s and bandwidth of 0.1 to 35 Hz. Other excitations included
172 aftershocks recorded after the 2018 Kumamoto earthquake and 2011 Tohoku earthquake that
173 represented smaller and more frequent earthquakes that occur on an annual basis in many parts of
174 Japan. This paper only discusses results from the JMA Kobe and white-noise excitations.

175 ***Instrumentation Plan***

176 Fig. 6 illustrates the instrumentations for floor accelerations and story drifts. The realized
177 ground acceleration was measured by two triaxial accelerometers placed at 2,500 mm from the
178 shake-table corners. At each floor, floor acceleration was measured by two triaxial accelerometers
179 placed at 600 mm from the corner columns. The story drifts in *Y*- and *X*-directions were measured
180 by two pairs of laser displacement sensors placed on rigid tables fixed to the floor below and
181 pointed at targets fixed to the floor above.

182 The interior columns at grid point 2C (Column 2C) of the 1st through 4th stories were
183 instrumented along with the panel zones and beams at the 3rd and 4th floors. Figs. 7(a) and (b)
184 show the instrumentation to obtain panel-zone shear deformations in *Y*- and *X*-directions, γ_Y and
185 γ_X, respectively. In each direction, shear deformation was measured as the relative displacement
186 between the top and bottom diaphragm plates, obtained from a pair of displacement transducers,
187 divided by the center-to-center distance between the diaphragm plates. The transducers were
188 placed on rigid holders glued to the bottom diaphragm plate in the *X*-direction and column surface
189 stiffened by an interior diaphragm in the *Y*-direction, and pointed at targets fixed to the upper
190 diaphragm plate. Fig. 7(c) shows strain gauges placed on Column 2C at the 1st through 4th stories
191 to enable deduction of biaxial bending moments and axial force. Displacement transducers, with a
192 gauge length from the slab surface to the lower diaphragm plate, were placed along Column 2C at
193 the 1st and 3rd stories to measure axial deformation. Figs. 7(d) and (e) show strain gauges placed

on the four beams connecting to Column 2C at the 3rd and 4th floors to enable deduction of beam bending moments. The beam bending moment was computed based on the curvature obtained from the strain gauges, assuming the slab axial force to act at mid thickness and equal the axial force in the steel beam, with the exception of Beam B2 in Fig. 7(d). For Beam B2, the bending moment was computed assuming the beam axial force to equal the horizontal component of the BRB axial force. Fig. 7(f) shows displacement transducers placed at the ends of the beams to measure rotation over a gauge length of 730 mm in the *Y*-direction and 500 mm in the *X*-direction. Beam end rotation, θ_b, was evaluated as the difference of measured displacements divided by the vertical distance between the transducers. Instrumentation of the BRB force and axial deformations is described by Fujiwara et al. (2024) and therefore omitted.

Deduction of Panel-Zone Shear Force

Fig. 8 shows the decomposition of free bodies used to compute the panel-zone shear force in the *X*-direction. As shown in Fig. 8(a), column and beam forces were sampled at mid-thickness of diaphragm plates and column surfaces, respectively. The subscripts in upper case "*L*", "*R*", and "*T*" stand for left, right, and top, lower case "*b*", "*c*", and "*BRB*" stand for bare steel, concrete slab, and BRB, and furthermore, "*f*" and "*w*" stand for flange and web, respectively. Positive bending moment (slab in compression) was decomposed using the method proposed by Kishiki et al. (2010), with one more assumption that beam neutral axis is fixed at elastic position. As discussed later, this beam remained elastic, and its elastic stiffness matched the evaluation based on the same assumed neutral axis position. As illustrated in Fig. 8(b), positive bending moment was decomposed into bending moment developed in the steel section, M_b, plus equal and opposite forces, F_c, at the centroid of steel beam and composite slab, while the negative bending moment

(slab in tension) was assumed to be taken by the steel section only. Axial compression in the slab was transferred to the upper column, and bending moment and axial force in the steel beam were translated into equivalent concentrated forces at the steel beam flanges. Fig. 8(c) shows the forces transferred to the panel zone converted to the equivalent shear force, V_X.

Fig. 9 shows the decomposition of free bodies used to compute the panel-zone shear force in the *Y*-direction. The free body in Fig. 9(a) was sampled differently from the previous case on the side with gusset plate: beam forces were evaluated at the section instrumented with strain gauges, and column forces were evaluated at the edge stiffeners of the gusset plate. The BRB was assumed to deliver axial force, N_{BRB}, only, and the horizontal component of the BRB force was assumed to be taken by the right beam only. Fig. 9(b) and (c) show how the forces in the beam and column segments stiffened by gusset plate were simplified. The left end of the beam segment included the steel beam, gusset plate, and horizontal stiffener, but neglected the floor slab assuming that all forces acting on the right end of the free body were transferred to the steel components through bearing against the edge stiffeners of the gusset plate. Normal stress was assumed to distribute linearly, and shear stress was assumed to distribute uniformly in the vertical plates (the gusset plate and beam web). At the right end, the axial force and bending moment in the steel beam, N_b and M_b, were computed by measured strain, and the axial force in the slab, F_c, was deduced as the difference between the horizontal component of BRB force and axial force in the steel beam. The column segment between the horizontal edge stiffener and upper diaphragm plate was subjected to forces from upper column and stresses from gusset plate, and the resultant forces at bottom were computed by equilibrium. Figs. 9(d) and (e) show the forces and stresses converted to the equivalent shear force, V_Y.

Experimental Results

Global Response

Fig. 10 shows the transition of natural periods for *Y*- and *X*-translation and torsion about the *Z*-axis identified from the white-noise excitations. The frequency response function (FRF) method (Ewins 2009) was used assigning the shake-table and roof floor accelerations as the input and output. The frequencies at the peaks of the imaginary part of the FRF were recognized as the natural frequencies. The fundamental vibration periods changed from the original 0.61 s, 0.82 s, 0.56 s (Test 01), respectively, for the *Y*-, *X*-translations, and torsion, to 0.68 s, 0.91 s, 0.63 s (Test 14) after the 100% motion. The primary motions, from 50% to 100% each caused elongation of the four periods in *X*- and *Y*-translations and torsion, and after the 100% motion, the periods had elongated by 5 to 10%.

Fig. 11 shows the maximum floor accelerations and maximum story drift ratios during the JMA Kobe motions, where the solid lines represent measured results and the dashed lines represent simulation results described in a later section. At the roof, floor acceleration was amplified by factors of 3.37 and 4.82 in the *Y*- and *X*-directions during the 25% motion, and 1.85 and 2.32 during the 100% motion. The specimen yielded over the lower stories in both *Y*- and *X*-directions. In the 3rd story, which showed the largest story drifts, the maximum story drift ratios were 0.020 rad in the *Y*-direction and 0.017 rad in the *X*-direction.

Beam Response

Fig. 12 shows the measured response of the four beams connecting to grid point 2C at the 3rd floor, plotting the beam-end bending moment versus rotation (within the aforementioned gauge length) during the 100% motion. This figure and subsequent figures plotting the measured hystereses indicate the state at the start and end of excitation. Some hystereses indicate notable damage accumulation. The theoretical elastic stiffness was calculated by integrating curvature over

the transducer gauge length, assuming rotations at two beam ends are identical. The positive stiffness, K_b^+, assumed the effective widths of concrete slabs as 950, 550, 750, and 500 mm for B1 to B4, respectively, per AIJ (2023), as the beam flange width plus $(1.0 - 1.2a/l_b)\cdot a$ when $a < 0.5l_b$; or $0.2l_b$ when $a \geq 0.5l_b$ for B1 and B3, and plus $(0.5 - 0.6a/l_b)\cdot a$ or $0.1l_b$ for B2 and B4 due to the slab opening in the middle, where a is the distance between the flanges of adjacent beams and l_b is the beam span. The negative stiffness, K_b^-, was computed based on the bare beam section. The positive plastic moment, M_p^+, was computed based on an assumed fully plastic state with the effective width of the concrete slab equals 1.3 times the column width per AIJ (2023). The negative plastic moment, M_p^-, was computed based on the bare beam section. The four beams responded elastically and did not develop plastic moment in positive or negative bending. The measured elastic stiffness agreed with the theoretical stiffness except for Beam B2, which showed larger stiffness than the theoretical, presumably because the theoretical value neglected the added stiffness due to BRB gusset plate.

Column Response

Fig. 13 shows the axial force versus axial deformation response of Column 2C at the 3rd and 1st stories during the 100% motion, where the positive values represent tension and elongation. Compression from gravity was estimated based on tributary area. At the 3rd story, the maximum axial force was -0.28 times the axial yield force and the maximum averaged strain was -0.83×10^{-3}. At the 1st story, the maximum axial force was -0.41 times the axial yield force and the maximum averaged strain was -1.07×10^{-3}.

Fig. 14 shows the column bending moments in *X*- and *Y*-planes, M_{cX}/M_{cp0} and M_{cY}/M_{cp0}, measured at the 3rd story during the 100% motion, where M_{cp0} denotes the column plastic moment under pure bending. Force trajectories were constructed for the top and bottom sections of the

column shown in Fig. 7(c). The indicated plastic limits were computed for a constant axial force that equals gravity load over tributary area. During the 100% motion, the force trajectories at both sections exceeded the plastic limits. After the 100% motion, little residual forces remained in this column, with residual lateral drift ratios of 0.003 rad and 0.001 rad in the *Y*- and *X*-directions, respectively.

Fig. 15 plots the transition of inflection point for the same column during the 100% motion for the durations when the column moment at either end was greater than 20% of the maximum measured moment. The average locations of inflection points are highlighted by dashed lines. In the *Y*-direction, the inflection point was above mid-height, presumably because the BRB gusset plate contributed to the rotational stiffness at the bottom end. In the *X*-direction, the inflection point was near mid-height as expected. The measured inflection point was utilized to calibrate a numerical model presented in a later section.

Panel Zone Response

Fig. 16 shows the *Y*- and *X*-responses of the panel zone at the 3rd floor of Column 2C measured during the 50% and 100% motions. The shear forces were deduced using the scheme described earlier. Per AIJ (2021), the elastic shear stiffness, K_v, was computed from Eq. (1) and the plastic shear strength, V_p, from Eq. (2) which is applicable when axial force is smaller than 0.5 times the axial yield force.

$$K_v = G\frac{A_c}{2} \tag{1}$$

$$V_p = 2d_c t_c \frac{F_{yp}}{\sqrt{3}} \tag{2}$$

In the above equations, G denotes the elastic shear modulus of steel; A_c the area of HSS section; d_c the depth of HSS section; t_c the thickness of HSS section; F_{yp} the yield strength of HSS section.

The measured elastic stiffnesses agreed with K_v, which validated the described force deduction scheme. During the 50% motion, the panel zone remained elastic in the *Y*-direction but slightly yielded in the *X*-direction. During the 100% motion, the panel zone showed notable plastic deformations in both directions. The shear angle reached 0.01 rad in the *X*-direction. At the end of the 100% motion, residual deformations of 0.002 rad remained in both directions. Interestingly, the maximum shear force in the *Y*-direction was lower than the plastic shear strength V_p. The reason is attributed to interaction between biaxial shear forces and column axial force as discussed next.

Force Interaction in Panel Zones

Interaction between biaxial shear forces and axial force in the panel zone may be derived from plasticity theory. The interaction equations derived by Arakida et al. (2019) for panel zones with identical height in both directions, as shown in Fig. 17(a), are reviewed in the Appendix. The panels parallel to the *Y*-direction are denoted *Y*-panels, and those parallel to the *X*-direction are denoted *X*-panels. As reported by Arakida et al. (2019), the critical condition generally occurs at the edge section shown in Fig. 17(b) unless axial force is extremely large (axial force ratio overs 0.9). As shown in Fig. 17(c), the panel zones of the building specimen had different heights between the *X*- and *Y*-panels, and the critical condition occurred at the top edge section where the biaxial moments were largest. To apply the equations derived by Arakida et al. (2019), it was assumed that the panel zone had identical height in two directions, and the larger *X*-panel height was chosen for Eqs. (A1) to (A3) to construct plastic limit. Larger beam heights lead to smaller shear strength in the panel zone to maintain the corresponding bending moment and normal stress at the top edge section.

Fig. 18 shows the biaxial shear forces in the panel zone at the 3rd floor of Column 2C measured from the 50% and 100% motions. The indicated plastic limit, which was nearly circular, assumed that the axial force remained constant at the maximum values, 0.24 and 0.28 times axial yield strength for the 50% and 100% motions, respectively. During the 50% motion, the panel reached the plastic strength twice with large shear in the *X*-panels but small shear in *Y*-panels. During the 100% motion, the biaxial shear forces exceeded the plastic limit multiple times by large margins. Points A and B marked the times when the *X*-panel developed the maximum negative and positive deformations. Figs. 16(c) and (d) indicate the plastic strengths computed from Eqs. (A1) to (A3) based on the n and θ at Points A and B. At Point A shown in Fig. 16(d), the overstrength ratio was 1.45. For the large shear force in the *X*-direction, the plastic strength in *Y*-direction decreased from V_p to $V_{pY,A}$ in Fig. 16(c), which might explain the *Y*-panel developed notable plasticity with shear force smaller than the expected shear strength V_p. A similar behavior was observed at Point B when the *X*-panel developed the maximum positive deformation.

Numerical Simulation

Modeling of beam-to-column joint with BRB connection

A BRB-to-beam-to-column joint model was calibrated based on 2D static pushover analysis of a fishbone model (Luco et al. 2003) centering Column 2C in the *Y*-direction. The OpenSees platform (OpenSees 2006) was used for the analysis. As shown in Fig. 19(a), the fishbone model comprised Column 2C, half-length of the east and west beams connecting to the column, and the left BRBs. The column was fixed at the base, and the beams were supported at their inflection points by rollers. Fig. 19(b) shows the member arrangement at the 7th and 8th floors where a BRB framed to the bottom of the column but not to the top. All beam-to-column

joints had their panel zone modeled with rigid bars arranged in parallelogram and connected by four hinges and a rotational spring as proposed by Gupta and Krawinkler (1999). The BRB was modeled by an elasto-plastic truss, two elastic beams and two rigid bars connected in series. The length and cross-section of the truss and elastic beams were based on the yielding segment and connection segments of the BRB core. The lower end of the BRB was rigidly connected to the panel zone. At BRB-to-beam-to-column joints, the gusset plate was represented by an elastic steel truss connecting the stiffened gusset corners, spanning length l_{et}, and assigned the same thickness as the gusset plate and width of a_{et} times l_{et}. The key to defining this truss is to examine an adequate factor a_{et}. The scheme follows the suggestions by Kaneko et al. (2008) and Kishiki et al. (2008) but does not necessarily reflect the force transfer mechanism expressed in Fig. 9. The column and beam outside the gusset plate were modeled by force-based beam-column elements with 6-point Gauss-Lobatto integration. Figs. 19(c) and (d) depict the fiber sections of composite beams and columns. The slab widths were taken as 950 mm for the left beams and 550 mm for the right beams per AIJ (2023). All steel components that could potentially yield, including beams, columns, and BRB cores, were represented by the Giuffre-Menegotto-Pinto model, and the concrete was represented by the Kent-Scott-Park model.

Elastic pushover analysis was conducted separately for the positive and negative directions to consider the difference in stiffness of the composite beams. As shown in Fig. 19(a), loading was applied in displacement control using the distributions of maximum floor drifts measured from the 25% motion. Analysis was repeated for models with different a_{et} varied from 0 to 1 with an increment of 0.1. Aspect ratio $a_{et} \geq 0.2$ resulted in mean absolute percentage error, in height of inflection point at the 2nd to 4th stories between experiment and simulation, smaller than 4%.

Time history analysis in the next section adopted a_{et} = 0.2 to match the measured elasto-plastic panel zone response. Further verification is warranted to determine the most suitable value for a_{et}.

Time history analysis

Two-dimensional nonlinear time history analysis was conducted to verify the proposed modeling scheme in the *Y*-direction, granted using model that was calibrated to match the measured response. Fig. 20 shows the numerical model with one exterior frame (Frame D) and one interior frame (Frame C) taking advantage of symmetry. The two frames were connected by rigid trusses at each floor to simulate rigid floor diaphragms. The same modeling schemes as in the pushover analysis were adopted. The effective width of the floor slab was 800 mm for Frame D. At each floor, half of the total floor mass was evenly assigned to the eight beam-to-column joints at the right nodes of the panel zones. Gravity load within tributary area was modeled as line load along the beams. Rayleigh damping with a critical damping ratio of 0.02 was assigned to the 1st and 3rd natural periods. Numerical integration over time was performed based on the average acceleration method and time increment of 0.01 s. Analysis was executed continuously using the realized 25%, 50%, 75% and 100% table motions, each lasting 40 s. A 60-s rest was set between the adjacent motions to eliminate free vibration.

Table 5 compares the natural periods, in which the measured periods are the same periods of Test 01 plotted in Fig. 10 and the simulated periods were obtained from eigenvalue analysis of the models. The model matched the measured 1st period, but overpredicted the 2nd to 4th periods. The simulated responses are plotted in Fig. 11 against the measured responses. The simulated floor accelerations agreed with the experiment up to the 75% motion, but underestimated the experiment at upper floors by 20% for the 100% motion. The simulated story drift ratios agreed with the experiment for the 25% to 75% motions but underestimated the story drift at upper stories by 25%

for the 100% motion. The difference in response between simulation and experiment was caused presumably by the different fixity at the column base. Comparison of simulated versus measured bending moment distribution indicated that the base fixity in experiment was smaller than fixed as assumed in simulation. The higher base fixity led to overestimated acceleration and underestimated deformation at bottom stories, which in turn, caused the difference in response at the upper stories.

Fig. 21 compares the simulated versus measured response of the panel zone of Column 2C at the 3rd floor during the 100% motion. The simulation consistently overestimated the response on the positive side (left beam, as seen in Fig. 9(a), in positive bending, and right beam in negative bending) and underestimated the response on the negative side. On the positive side, the simulated shear force overestimated the measured by as much as 60%, presumably because the left beam was modeled with a wider effective slab than the right beam, and consequently, possessed a much larger strength capacity in positive bending than the right beam did. Furthermore, the model was unable to capture the reduction in plastic strength caused by loading in the orthogonal frame. Further modification for the panel zone model is warranted to incorporate the interaction effect described in the paper. Modification is also warranted in the definition of effective width in composite slab models.

Conclusions

Shake-table tests of a nearly-full-scale, 10-story steel MRF with BRBs were conducted. The interior columns and panel zones along with BRBs yielded under bidirectional dynamic loading to produce maximum story drift ratio of 0.02 rad in both orthogonal directions. The measured responses presented challenges in modeling the inelastic behavior of square-HSS panel zones under realistic conditions: interaction of bidirectional forces, stiffening due to a BRB gusset

plate, presence of composite slab among other factors. An attempt was made to express the force transfer mechanism and thereby the force demand imposed in panel zones, to derive the strength interaction in square-HSS panel zones, and to model square-HSS panel zones in structural frame analysis. Key findings from the study are summarized below:

1. Even after developing maximum story drift ratios of 0.020 and 0.017 rad in the two orthogonal directions, the natural periods of the specimen increased by merely 10% from the undamaged state. Therefore, the program provided another proof that the elastic stiffness of steel building systems remains rather consistent after experiencing moderate damage.

2. The presented method to deduce shear force acting on panel zones resulted in reasonable match between measured and theoretical stiffness of the panel zone. Therefore, although further study is warranted, this method may be used to account for reduction in shear force demand due to composite slabs and bracing connections.

3. The measured response of the panel zones was clearly affected by force interaction due to bidirectional loading. The plasticity model by Arakida et al. (2019) was confirmed as a useful mean to understand this force interaction.

4. The simple modeling scheme to represent stiffening due to bracing connections by a short truss between the beam and column elements was, after calibration, able to capture elasto-plastic panel-zone shear deformation. Further study is warranted to examine the general applicability of this modeling scheme and to develop refined models that can capture the force transfer mechanism and force interaction at panel zones.

Appendix. Panel Zone Strength Derived by Arakida et al. (2019)

Arakida et al. (2019) derived the plastic strength of panel zones in square-HSS columns. An isolated panel zone, as shown in Fig. 17(a), was examined at the edge section near the diaphragm plate and mid-height. Arakida et al. (2019) deduced that the edge sections generally provide a more critical condition than the mid-height section. Therefore, this appendix only discusses the edge section. Fig 17(b) shows the top edge section subjected to axial force, biaxial shear forces, and biaxial bending moments. Normal stresses and shear stress in the *Y*- and *X*-panels are related to the forces through equilibrium assuming uniform stress distribution. Two normal stresses are considered: σ_Z produced by axial force and bending moment, and σ_X due to constraint by the diaphragm plate. Relationship between σ_X and σ_Z is assumed fixed as $\sigma_X = 0.5\sigma_Z$. Equilibrium and Mises yield criteria between the stresses are used to derive lower-bound interaction equations between the axial force and biaxial shear forces. With axial force ratio $n = N/N_y$, where N is the axial force and N_y is the axial yield strength, the plastic shear strength in θ direction, $V_{p\theta}$, is expressed by Eqs. (A1) to (A3). Eq. (A3) is an implicit function which can be solved numerically. $V_{p\theta}$ is decomposed into *X*- and *Y*-components to construct the full interaction diagram between the plastic strengths in *X*- and *Y*-directions.

(a) $0 \le l/d_c \le 2$ and $0 \le n \le n_{bX}$:

$$\frac{V_{p\theta}}{V_p} = \frac{1}{\sqrt{\frac{1}{4}\left(\frac{l}{d_c}\right)^2 \sin^2\theta + \cos^2\theta}} \tag{A1}$$

(b) $2 < l/d_c$ and $0 \le n \le n_{bY}$:

$$\frac{V_{p\theta}}{V_p} = \frac{1}{\sqrt{\frac{1}{4}\left(\frac{l}{d_c}\right)^2 \cos^2\theta + \sin^2\theta}} \tag{A2}$$

(c) $n_{bX} < n \le 1$ and $n_{bY} < n \le 1$:

$$n = -\frac{l(\sin\theta + \cos\theta)}{2\sqrt{3}d_c}\frac{V_{p\theta}}{V_p} + \frac{1}{\sqrt{3}}\left[\sqrt{1 - \left(\frac{V_{p\theta}}{V_p}\right)^2 \sin^2\theta} + \sqrt{1 - \left(\frac{V_{p\theta}}{V_p}\right)^2 \cos^2\theta}\right] \tag{A3}$$

In the above equations, l denotes the clear distance between the upper and lower diaphragm plates; n_{bX} and n_{bY} are the critical axial force ratios that distinguish the cases, expressed respectively by Eqs. (A4) and (A5).

$$n_{bX} = \frac{-\frac{l\cos\theta}{2d_c} + \sqrt{\left[\left(\frac{l}{2d_c}\right)^2 - 1\right]\sin^2\theta + \cos^2\theta}}{\sqrt{3\left[\left(\frac{l}{2d_c}\right)^2 \sin^2\theta + \cos^2\theta\right]}} \tag{A4}$$

$$n_{bY} = \frac{-\frac{l\sin\theta}{2d_c} + \sqrt{\left[\left(\frac{l}{2d_c}\right)^2 - 1\right]\cos^2\theta + \sin^2\theta}}{\sqrt{3\left[\left(\frac{l}{2d_c}\right)^2 \cos^2\theta + \sin^2\theta\right]}} \tag{A5}$$

Data Availability Statement

Some or all data, models, or code that support the findings of this study are available from the corresponding author upon reasonable request.

Acknowledgments

The shake-table tests were conducted by the National Institute of Earth Science and Disaster Resilience of Japan. Collection of the reported data was made possible by JSPS KAKENHI Grant Number 20H00269. The first author was supported by Japanese Government (Monbukagakusho: MEXT) scholarship. The authors thank Nippon Steel Engineering Co., Ltd. for providing the BRBs, and Professor Noriyuki Takahashi and Professor Tomohiro Matsumiya for providing essential instrumentations. Professor Dimitrious Lignos provided valuable input on instrumentation plan and interpretation of panel zone behavior. Professor Amit Kanvinde provided

guidance in numerical analysis. Special thank is extended to the many graduate students at Nagoya University and Hokkaido University who helped prepare and install the instruments. The opinions expressed in this paper are those of the authors and do not necessarily reflect the views of the above-mentioned organizations, funding sources or individuals.

References

AIJ (Architecture Institute of Japan). 2021. *Recommendations for design of connections in steel structures.* [In Japanese.] Tokyo: AIJ.

AIJ (Architecture Institute of Japan). 2023. *Design recommendations for composite constructions.* [In Japanese.] Tokyo: AIJ.

AISC (American Institute of Steel Construction). 2016c. *Specification for structural steel buildings.* ANSI/AISC 360-16. Chicago: AISC.

Arakida R., I. Chan, and Y. Koetaka. 2019. "Full plastic strength of square hollow section panel zone under arbitrary directional shear force." [In Japanese.] *J. Struct. Constr. Eng.*, 84 (755), 85-95. https://doi.org/10.3130/aijs.84.85.

Elkady, A., and D. G. Lignos. 2014. "Modeling of the composite action in fully restrained beam-to-column connections: Implications in the seismic design and collapse capacity of steel special moment frames." *Earthquake Eng. Struct. Dyn.*, 43(13), 1935–1954. https://doi.org/10.1002/eqe.2430.

El Jisr, H., M. Kohrangi, and D. G. Lignos. 2022. "Proposed nonlinear macro-model for seismic risk assessment of composite-steel moment resisting frames." *Earthquake Eng. Struct. Dyn.*, 51(5), 1180–1200. https://doi.org/10.1002/eqe.3610.

Ewins, D. J. 2009. *Modal testing: theory, practice and application.* West Sussex, UK: John Wiley & Sons.

Fujiwara, J., T. Nagae, T. Yan, J. Jin, J. Li, T. Okazaki, A. Kishida, R. Nishi, K. Kajiwara. 2024. "3-D detailed finite element analysis of full-scale shaking table test on a 10-story steel building." In *Proc., 18th World Conf. on Earthquake Engineering*, Milan.

Gupta, A., and Krawinkler, H. 1999. *Seismic demands for the performance evaluation of steel moment resisting frame structures.* Report No. 132, The John A. Blume Earthquake Engineering Center, Stanford University, Stanford, California.

Hsiao, P. C., D. E. Lehman, and C. W. Roeder. 2013. "A model to simulate special concentrically braced frames beyond brace fracture." *Earthquake Eng. Struct. Dyn.*, 42(2), 183–200. https://doi.org/10.1002/eqe.2202.

Kaneko, K., K. Kasai, S. Motoyui, T. Sueoka, Y. Azuma, and Y. Ooki. 2008. "Analysis of beam-column-gusset components in 5-story value-added frame." In *Proc., 14th World Conf. on Earthquake Engineering*, Beijing.

Kasai, K., and Y. Matsuda. 2015. "Seismic Behavior of Composite Beams under Damper and Frame Forces of Shifted Phases: Finding from Full-Scale Tests of Buildings and Subassemblies." In *Proc., 6th International Conference on Advances in Experimental Structural Engineering*, Urbana.

Kim, K. D., and M. D. Engelhardt. 2002. "Monotonic and cyclic loading models for panel zones in steel moment frames." *J. Constr. Steel Res.*, 58(5-8), 605-635. https://doi.org/10.1016/S0143-974X(01)00079-7.

Kishiki, S., Y. Ichikawa, S. Yamada, and A. Wada. 2007. "Experimental evaluation of structural behavior of gusset-plate connection: Global enhancement of seismic performances of passive-

509 controlled structures Part 1." [In Japanese.] *J. Struct. Constr. Eng.*, 72(620), 133-140.
510 https://doi.org/10.3130/aijs.72.133_4.
511 Kishiki, S., M. Uekusa, and A. Wada. 2008. "Experimental evaluation of structural behavior of
512 steel member affected by the presence of gusset plate: Global enhancement of seismic
513 performance of passive-controlled structures Part 2." [In Japanese.] *J. Struct. Constr. Eng.*,
514 73(633), 2027-2036. https://doi.org/10.3130/aijs.73.2027.
515 Kishiki, S., D. Kadono, K. Satsukawa, S. Yamada. 2010. "Consideration of composite effects on
516 elasto-plastic behavior of panel zone." [In Japanese.] *J. Struct. Constr. Eng.*, 75(654), 1527-
517 1536. https://doi.org/10.3130/aijs.75.1527.
518 Li, J., J. Fujiwara, K. Kajiwara, A. Kishida, R. Nishi, T. Okazaki, T. Nagae, J. Jin, and T. Asai.
519 2024. "Panel zone and column response in a shake-table test on a 10-story steel moment-
520 resisting frame." In *Proc., 18th World Conf. on Earthquake Engineering*, Milan.
521 Luco, N., Y. Mori, Y. Funahashi, C. A. Cornell, and M. Nakashima. 2003. "Evaluation of
522 predictors of non-linear seismic demands using 'fishbone' models of SMRF buildings."
523 *Earthquake Eng. Struct. Dyn.*, 32(14), 2267–2288. https://doi.org/10.1002/eqe.331.
524 MLIT (Ministry of Land, Infrastructure, Transport and Tourism). 2020. *Commentary on Structural*
525 *Regulations of the Building Design Standard Law of Japan*. [In Japanese.] Tokyo: Official
526 Gazzete Co-operation of Japan.
527 Mojiri, S., P. Mortazavi, O. Kwon, C. Christopoulos. 2021. "Seismic response evaluation of a five-
528 story buckling-restrained braced frame using multi-element pseudo-dynamic hybrid
529 simulations." *Earthquake Eng. Struct. Dyn.*, 50(12), 3243–3265.
530 https://doi.org/10.1002/eqe.3508.
531 OpenSees. 2006. "Open System for Earthquake Engineering Simulation - Home Page" Accessed

November 30, 2023. http://opensees.berkeley.edu.

Skiadopoulos, A., A. Elkady, and D. G. Lignos. 2021. “Proposed panel zone model for seismic design of steel moment-resisting frames.” *J. Struct. Eng.*, 147(4): 04021006. https://doi.org/10.1061/(ASCE)ST.1943-541X.0002935.

Suita, K., S. Yamada, M. Tada, K. Kasai, Y. Matsuoka, and Y. Shimada. 2008. “Collapse experiment on 4-story steel moment frame: Part 2 detail of collapse behavior.” In *Proc., 14th World Conf. on Earthquake Engineering*, Beijing.

Wang, Y., R. Arakida, I. Chan, Y. Koetaka, and T. Nakano. 2018. “Cyclic behavior of panel zone in beam-column subassemblies subjected to bidirectional loading.” *J. Constr. Steel Res.*, *143*, 32–45. https://doi.org/10.1016/j.jcsr.2017.12.017.

Yamada, S., K. Satsukawa, S. Kishiki, Y. Shimada, Y. Matsuoka, K. Suita. 2009. “Elasto-plastic behavior of panel zone in beam to external column connection with concrete slab.” [In Japanese.] *J. Struct. Constr. Eng.*, 74 (644), 1841-1849. https://doi.org/10.3130/aijs.74.1841.

Table 1. List of columns (steel grade: BCR295)

Story	C1, C2	C3
10S-8S	Square-HSS-350×350×9	Square-HSS-250×250×6
7S	Square-HSS-350×350×12	Square-HSS-250×250×6
6S, 5S	Square-HSS-350×350×12	Square-HSS-250×250×9
4S-1S	Square-HSS-350×350×16	Square-HSS-250×250×9

Table 2. List of beams (steel grade: SN400B)

Floor	G1, G2, G4, G5	G3
RF-6F	H-350×175×7×11	H-244×175×7×11
5F-2F	BH-350×200×9×12	H-244×175×7×11

Table 3. Mechanical properties of columns, beams and BRBs

Component	Steel grade	Yield strength [N/mm^2]	Tensile strength [N/mm^2]	Elongation [%]
Square-HSS-350×350×9	BCR295	370	446	24.7
Square-HSS-350×350×12		381	443	26.3
Square-HSS-350×350×16		414	481	22.7
Square-HSS-250×250×6		391	458	38.8
Square-HSS-250×250×9		384	445	22.2
H-350×175×7×11, flange	SN400B	307	459	30.8
H-350×175×7×11, web		364	479	29.7
BH-350×200×9×12, flange		275	426	35.1
BH-350×200×9×12, web		291	431	33.7
H-244×175×7×11, flange		310	440	33.4
H-244×175×7×11, web		346	454	42.1
BRB core	LY225	214	302	41.0

555 **Table 4.** Summary of test cases

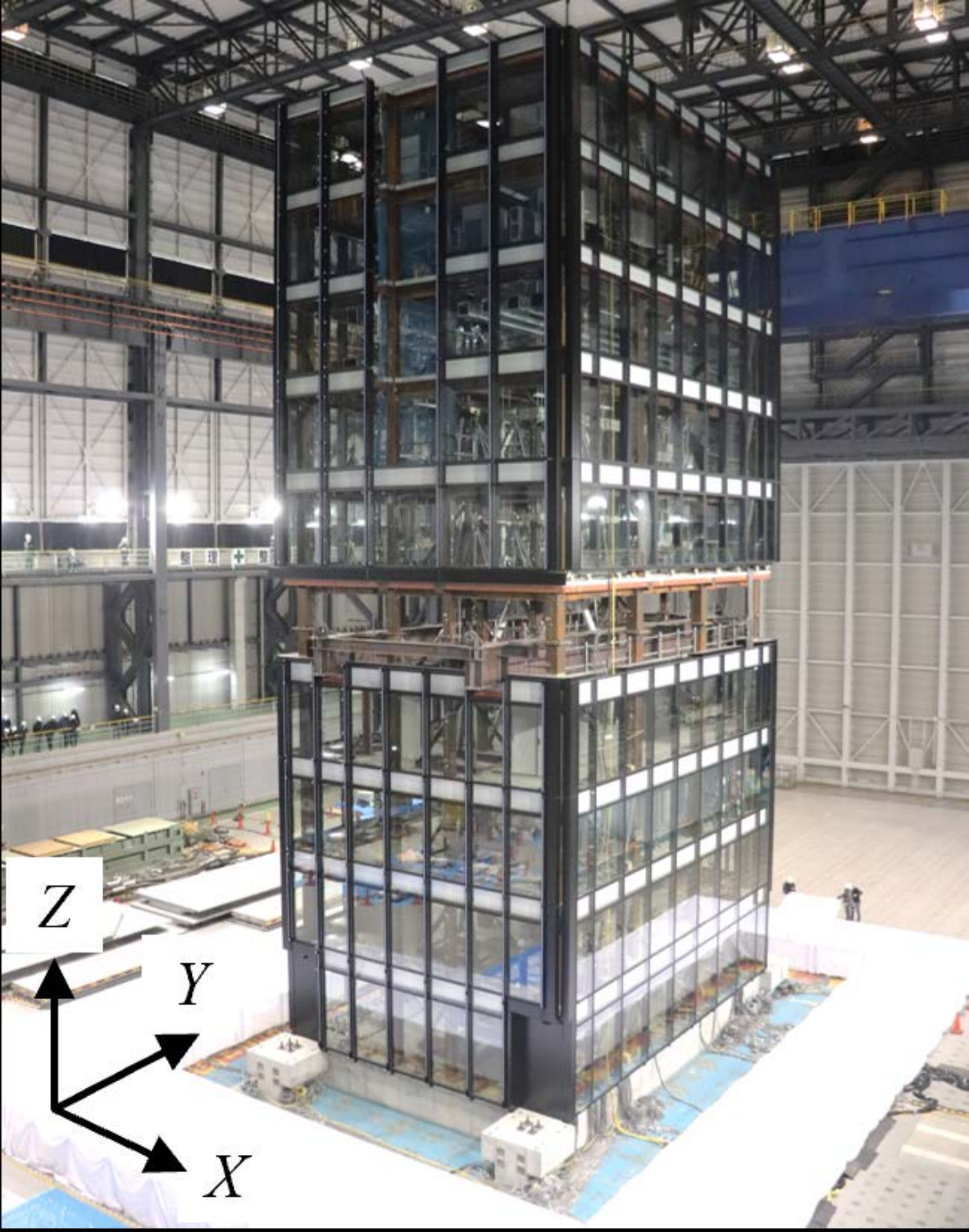
Test	Ground motion	Input direction
01	White-noise	*XYZ*
02	Kumamoto aftershock	*XYZ*
03	Tohoku aftershock	*XYZ*
04	Kobe 25%	*XYZ*
05	Kobe 25%	*X*
06	Kobe 25%	*Y*
07	Kobe 50%	*XYZ*
08	White-noise	*XYZ*
09	Kobe 75%	*XYZ*
10	White-noise	*XYZ*
11	Kumamoto aftershock	*XYZ*
12	Tohoku aftershock	*XYZ*
13	Kobe 100%	*XYZ*
14	White-noise	*XYZ*
15	Kumamoto aftershock	*XYZ*
16	Tohoku aftershock	*XYZ*

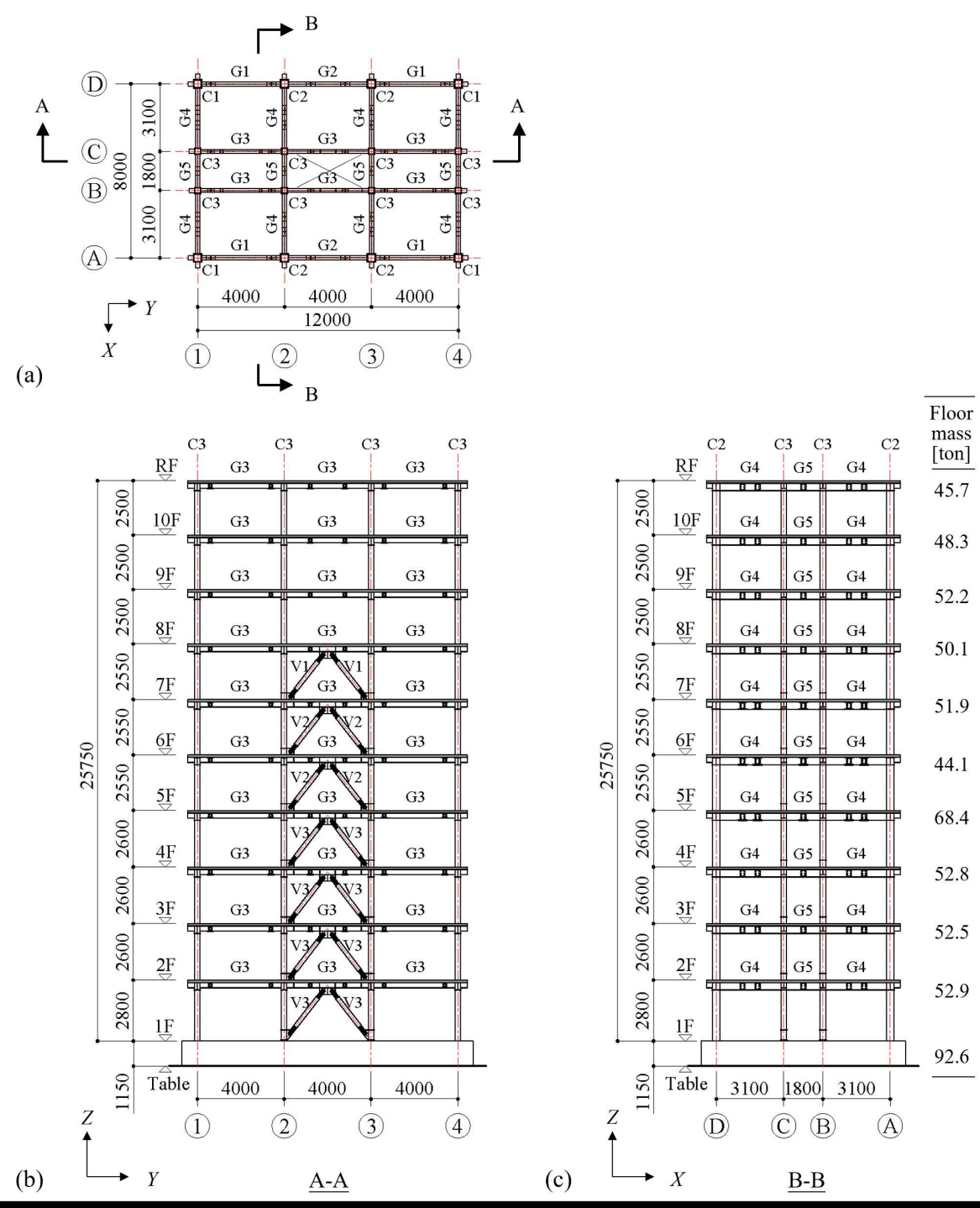
556

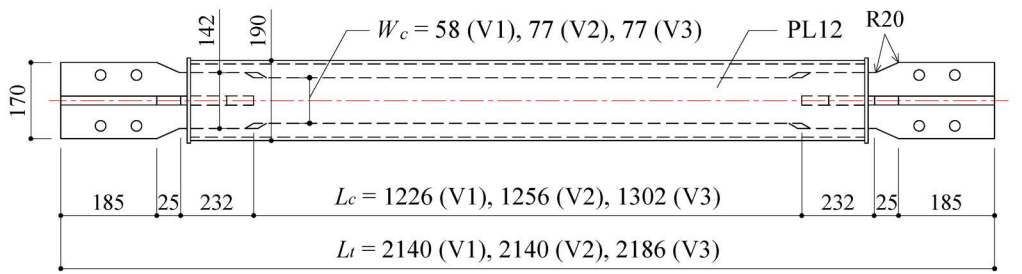
557 **Table 5.** Comparison of measured and simulated natural periods

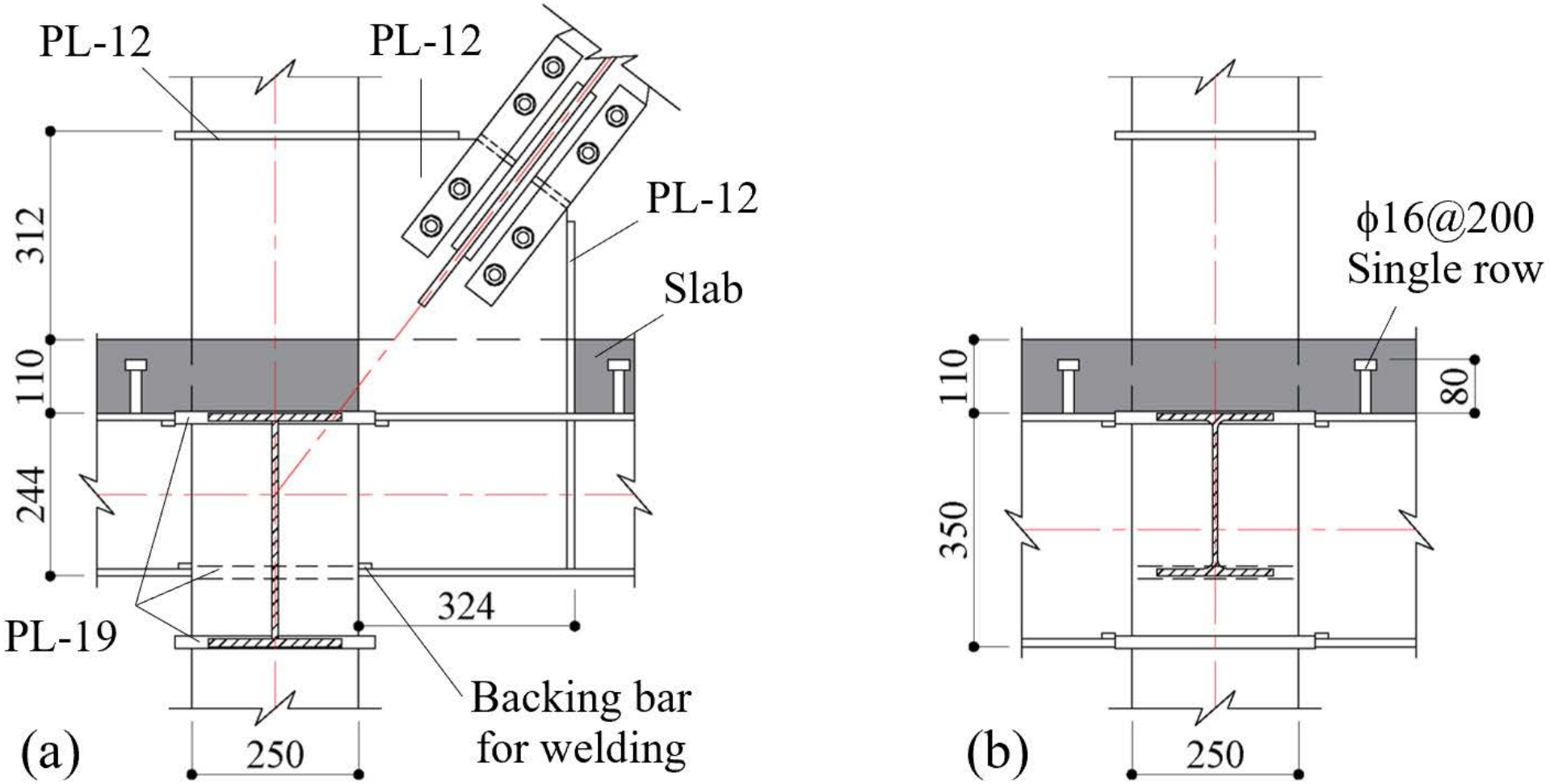
Mode in *Y*-direction	Measured [s]	Simulated [s]
1st	0.607	0.588
2nd	0.193	0.216
3rd	0.109	0.123
4th	0.072	0.084

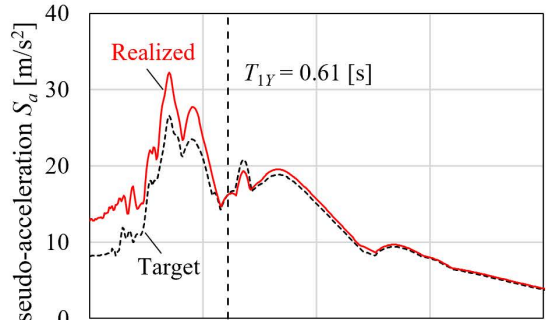
558


Z
Y
X

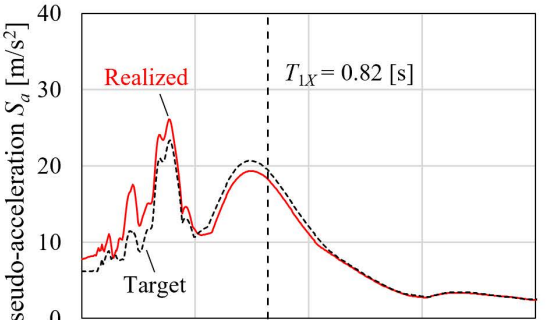

(a)
B
A
A
B
D
C
B
A
G1
G2
G1
C1
C2
C2
C1
G4
G3
G5
3100
1800
3100
8000
4000
4000
4000
12000
Y
X
1
2
3
4
(b)
C3
RF
10F
9F
8F
7F
6F
5F
4F
3F
2F
1F
Table
V1
V2
V3
2500
2550
2600
2800
1150
25750
4000
Z
Y
A-A
(c)
C2
C3
G4
G5
Floor mass [ton]
45.7
48.3
52.2
50.1
51.9
44.1
68.4
52.8
52.5
52.9
92.6
3100
1800
D
C
B
A
Z
X
B-B


142
190
W_c = 58 (V1), 77 (V2), 77 (V3)
PL12
R20
170
185
25
232
L_c = 1226 (V1), 1256 (V2), 1302 (V3)
232
25
185
L_t = 2140 (V1), 2140 (V2), 2186 (V3)

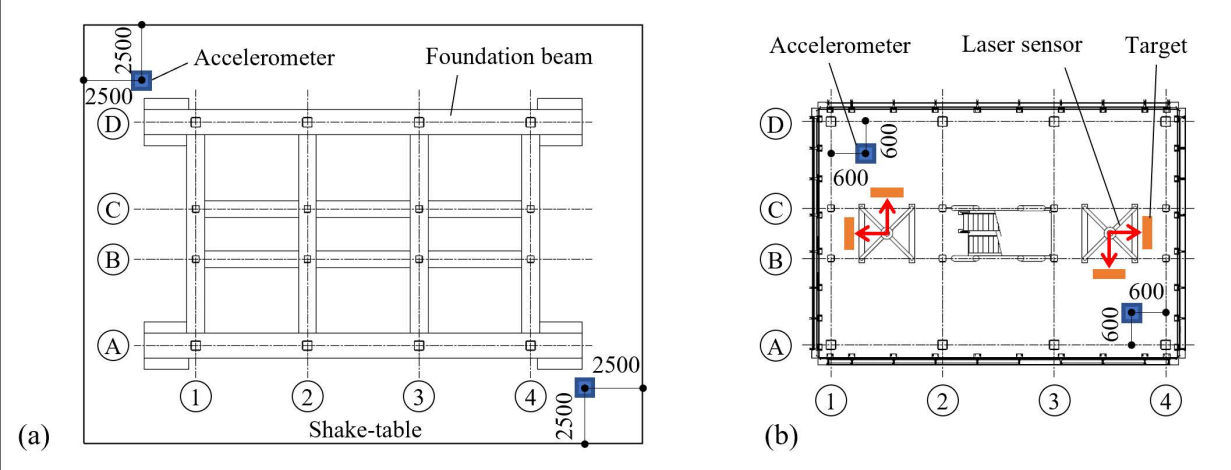

PL-12
PL-12
PL-12
Slab
312
110
244
PL-19
324
Backing bar
for welding
250
(a)
ϕ16@200
Single row
110
80
350
250
(b)

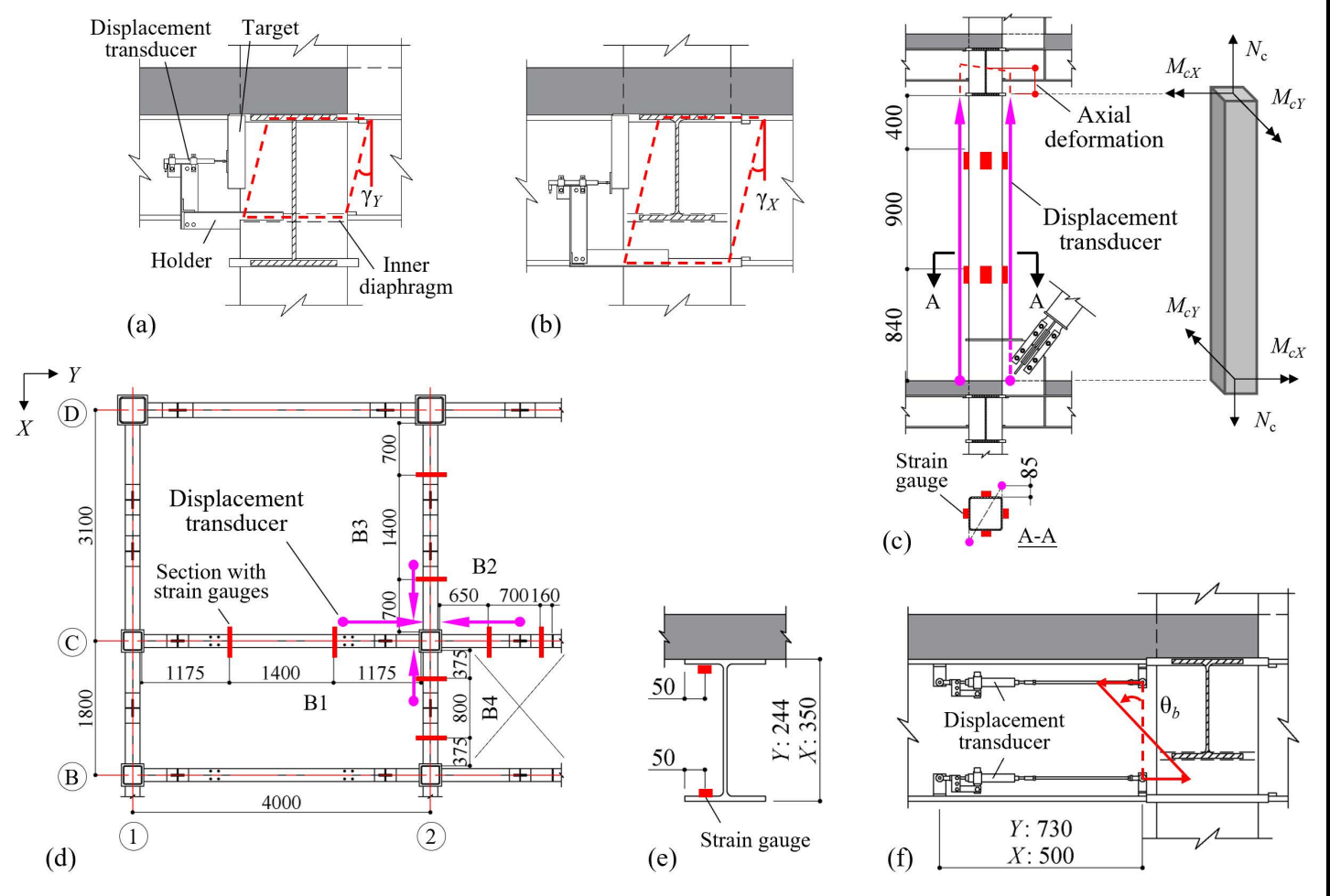

Realized
T_{1Y} = 0.61 [s]
Target
Pseudo-acceleration S_a [m/s^2]
Period T [s]
0
10
20
30
40
0
0.5
1
1.5
2

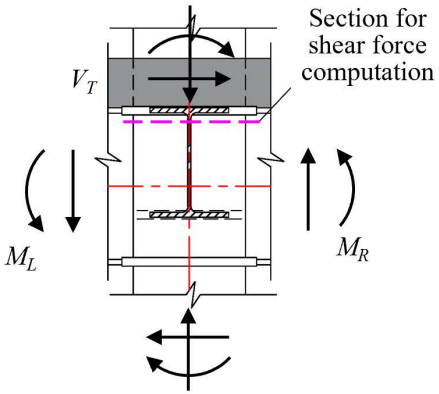
(a)


Realized
T_{1X} = 0.82 [s]
Target
Pseudo-acceleration S_a [m/s^2]
Period T [s]
0
10
20
30
40
0
0.5
1
1.5
2

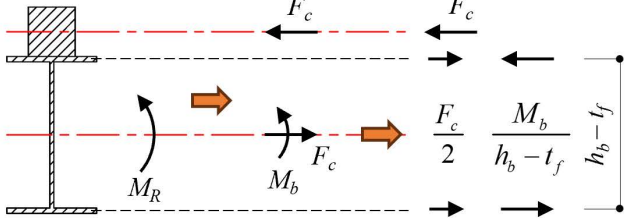
(b)


Accelerometer
Foundation beam
2500
2500
D
C
B
A
1
2
3
4
2500
2500
Shake-table
(a)
Accelerometer
Laser sensor
Target
600
600
600
600
(b)

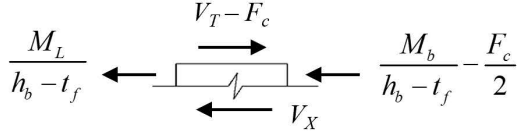

Displacement transducer
Target
Holder
Inner diaphragm
γ_Y
γ_X
(a)
(b)
N_c
M_{cX}
M_{cY}
Axial deformation
Displacement transducer
400
900
840
A
A
Strain gauge
85
A-A
(c)
Y
X
D
C
B
1
2
3100
1800
4000
700
1400
700
B3
B2
650
700
160
B1
1175
1400
1175
375
800
375
B4
Displacement transducer
Section with strain gauges
(d)
50
50
Y: 244
X: 350
Strain gauge
(e)
θ_b
Displacement transducer
Y: 730
X: 500
(f)


Section for
shear force
computation
V_T
M_L
M_R

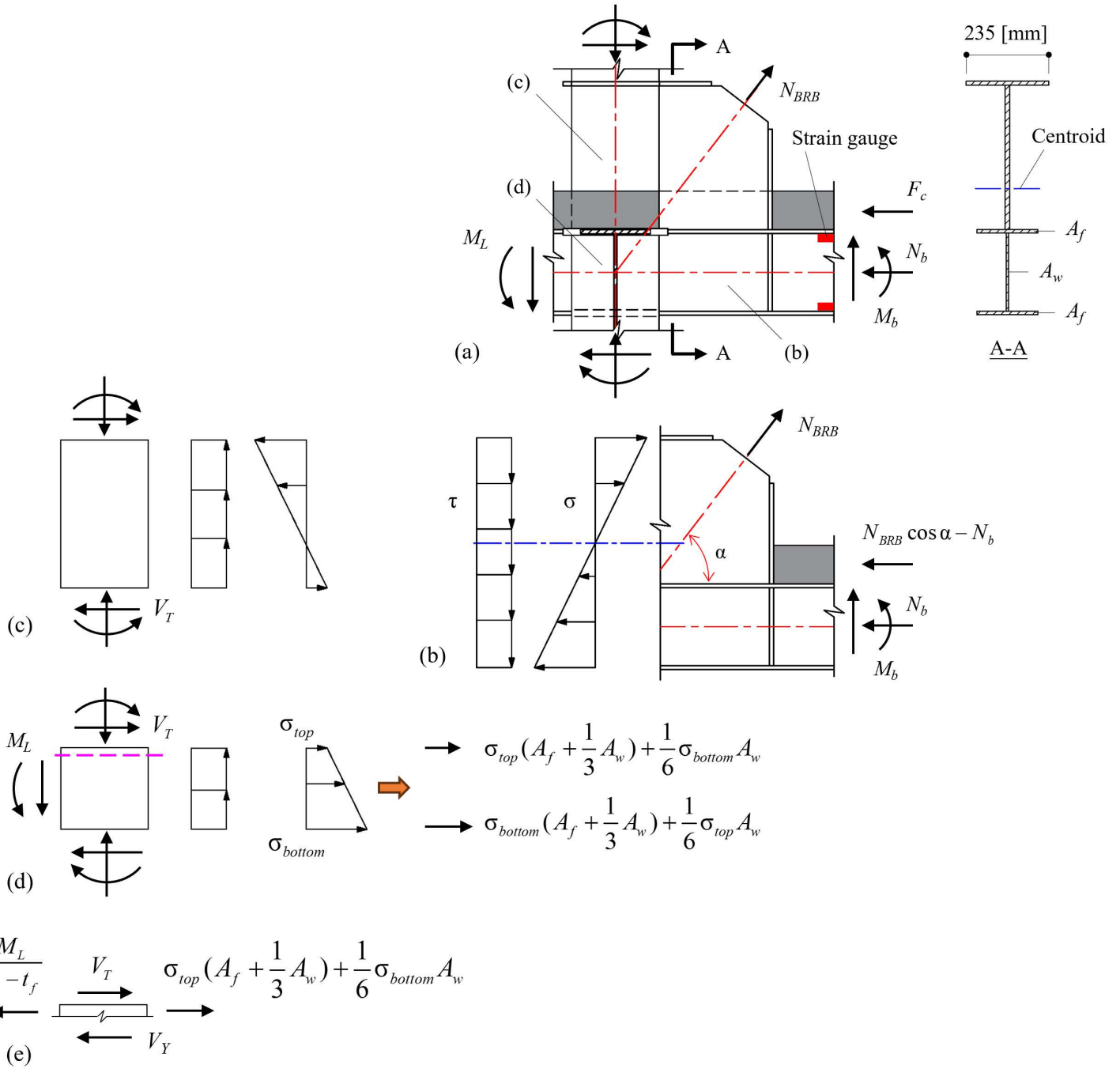
(a)

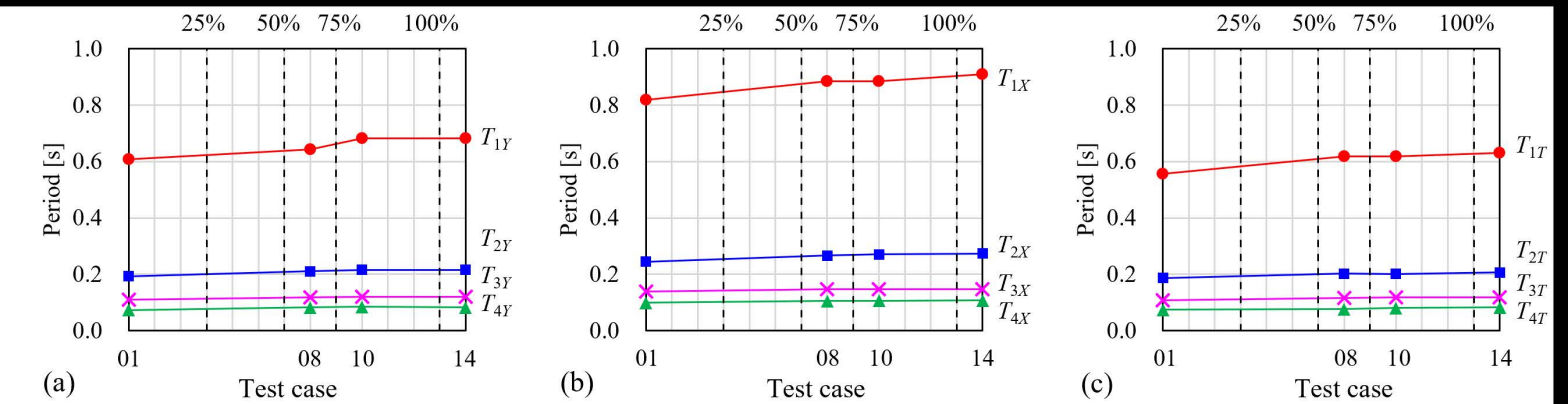

F_c
F_c
F_c
M_R
M_b
$\frac{F_c}{2}$
$\frac{M_b}{h_b - t_f}$
$h_b - t_f$

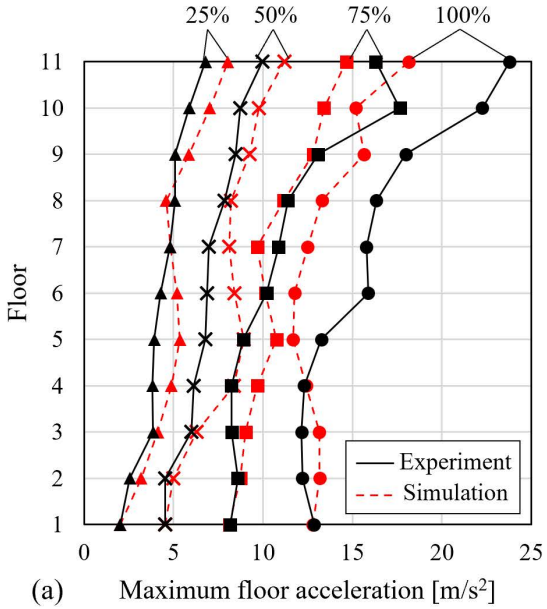
(b)


$V_T - F_c$
$\frac{M_L}{h_b - t_f}$
$\frac{M_b}{h_b - t_f} - \frac{F_c}{2}$
V_X

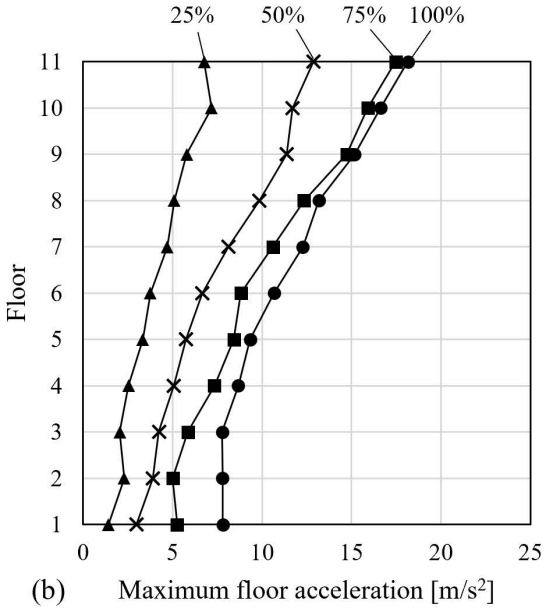
(c)


235 [mm]
A
(c)
N_{BRB}
Strain gauge
Centroid
(d)
F_c
M_L
N_b
A_f
A_w
M_b
A_f
(a)
A
(b)
A-A
N_{BRB}
τ
σ
$N_{BRB}\cos\alpha - N_b$
α
N_b
(b)
M_b
(c)
V_T
M_L
V_T
σ_{top}
σ_{bottom}
(d)
$\rightarrow \sigma_{top}(A_f + \frac{1}{3}A_w) + \frac{1}{6}\sigma_{bottom}A_w$
$\rightarrow \sigma_{bottom}(A_f + \frac{1}{3}A_w) + \frac{1}{6}\sigma_{top}A_w$
$\frac{M_L}{h_b - t_f}$
V_T
$\sigma_{top}(A_f + \frac{1}{3}A_w) + \frac{1}{6}\sigma_{bottom}A_w$
V_Y
(e)

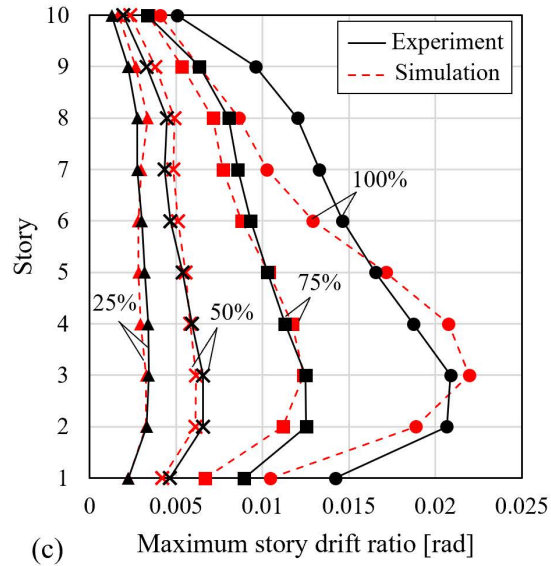

25%
50%
75%
100%
1.0
0.8
0.6
0.4
0.2
0.0
Period [s]
T_{1Y}
T_{2Y}
T_{3Y}
T_{4Y}
01
08
10
14
Test case
(a)
T_{1X}
T_{2X}
T_{3X}
T_{4X}
(b)
T_{1T}
T_{2T}
T_{3T}
T_{4T}
(c)


25%
50%
75%
100%
Floor
Experiment
Simulation
Maximum floor acceleration [m/s²]

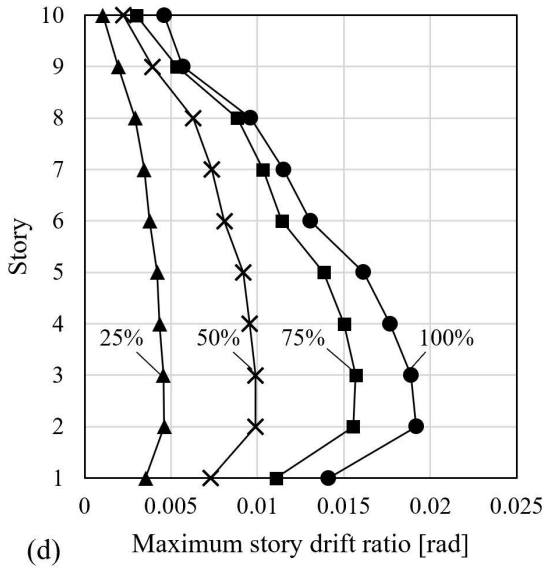
(a)


25%
50%
75%
100%
Floor
Maximum floor acceleration [m/s²]

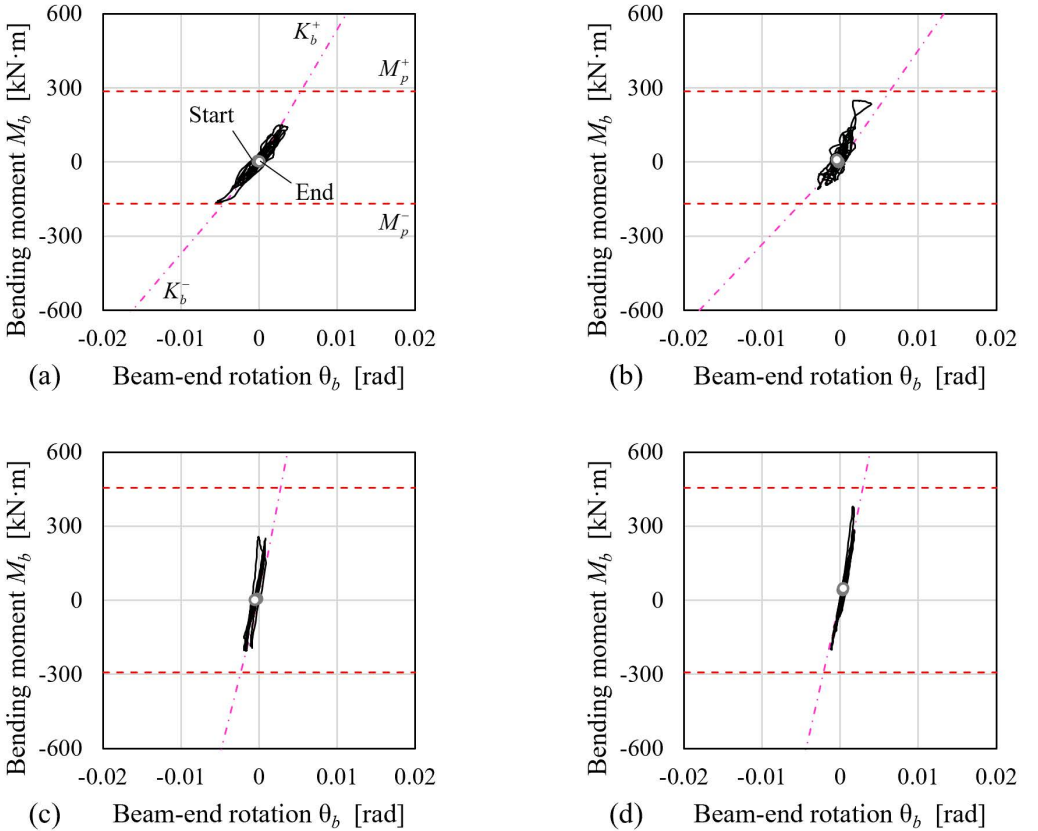
(b)

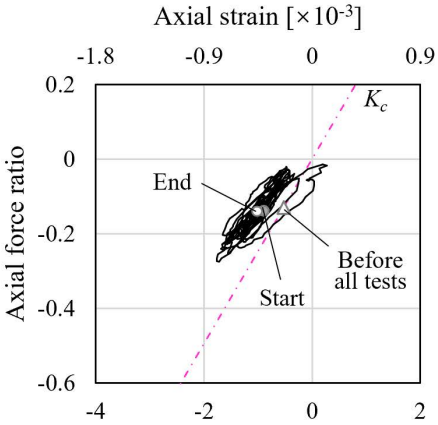

Experiment
Simulation
100%
75%
50%
25%
Story
Maximum story drift ratio [rad]

(c)

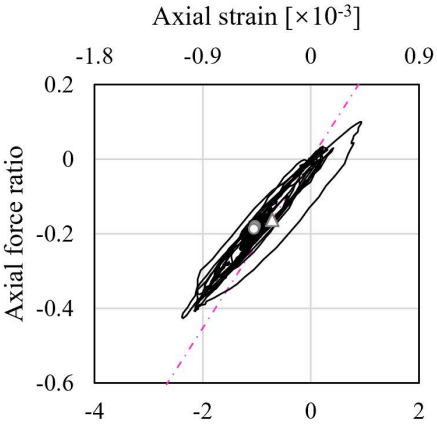

25%
50%
75%
100%
Story
Maximum story drift ratio [rad]

(d)

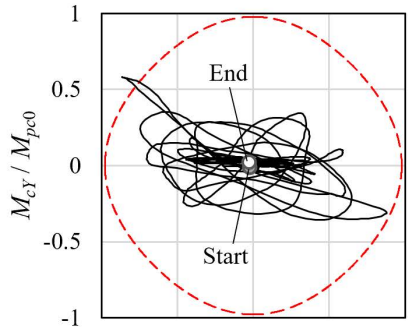

600
300
0
-300
-600
-0.02
-0.01
0
0.01
0.02
Bending moment M_b [kN·m]
Beam-end rotation θ_b [rad]
K_b^+
K_b^-
M_p^+
M_p^-
Start
End
(a)
(b)
(c)
(d)


Axial strain [×10-3]
-1.8
-0.9
0
0.9
0.2
0
-0.2
-0.4
-0.6
Axial force ratio
Kc
End
Start
Before
all tests
-4
-2
0
2
Axial deformation [mm]

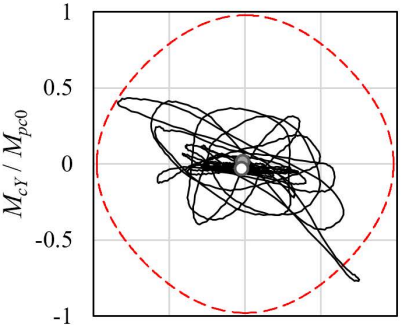
(a)


Axial strain [×10-3]
-1.8
-0.9
0
0.9
0.2
0
-0.2
-0.4
-0.6
Axial force ratio
-4
-2
0
2
Axial deformation [mm]

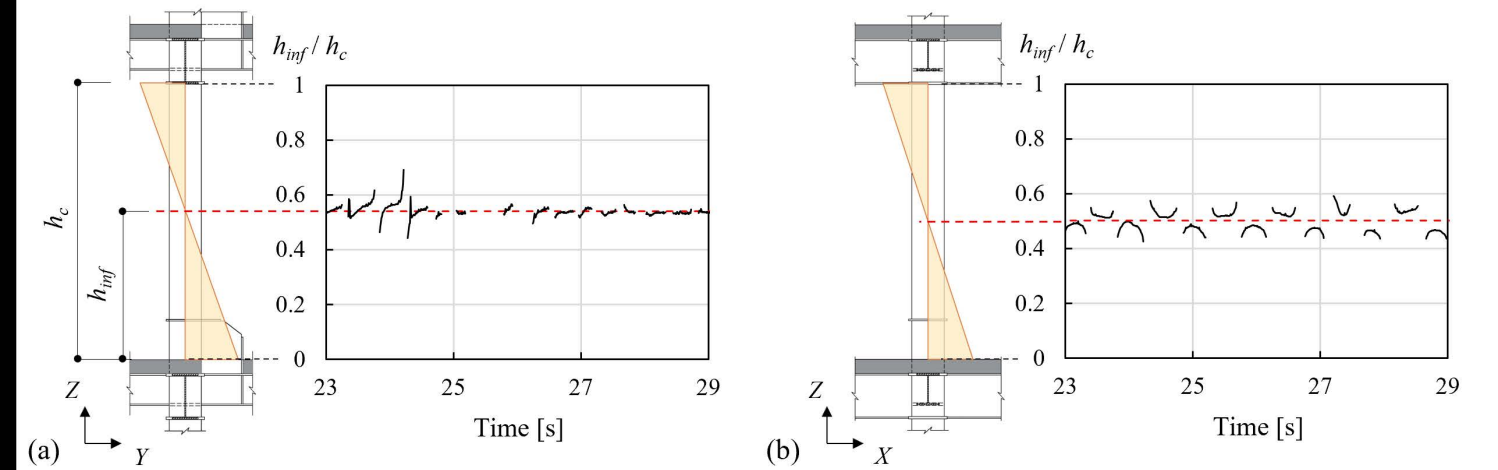
(b)

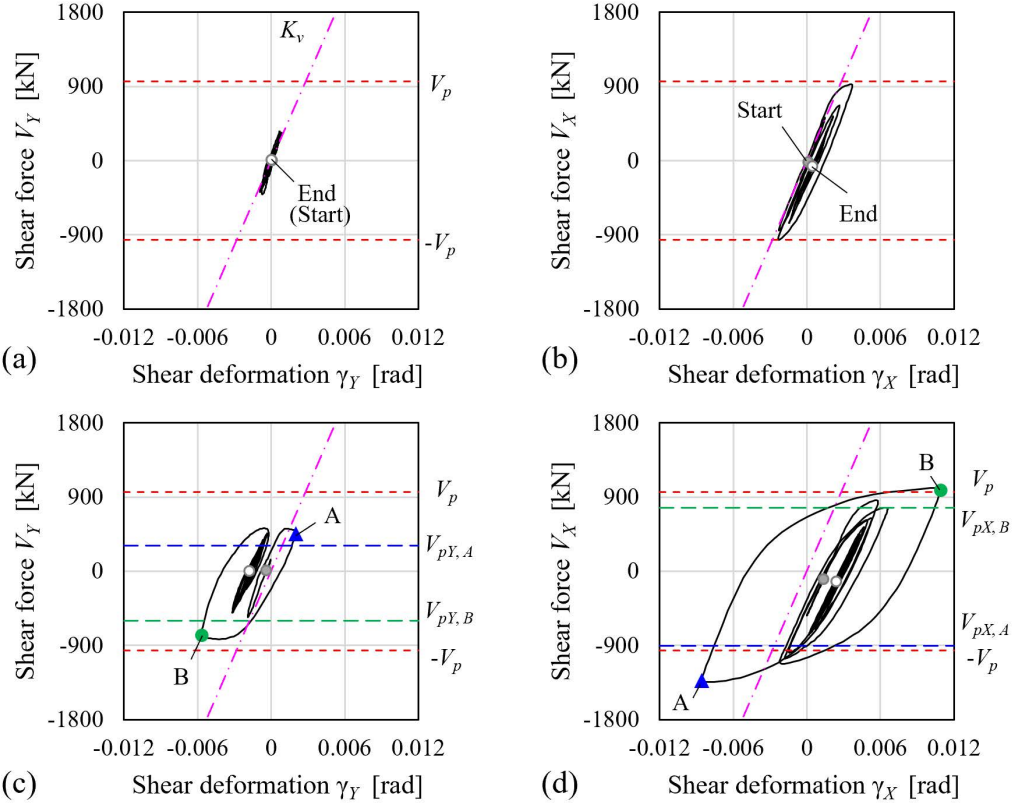

End
Start
1
0.5
0
-0.5
-1
M_{cY} / M_{pc0}
M_{cX} / M_{pc0}

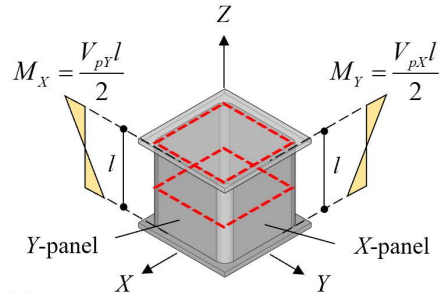
(a)


1
0.5
0
-0.5
-1
M_{cY} / M_{pc0}
M_{cX} / M_{pc0}

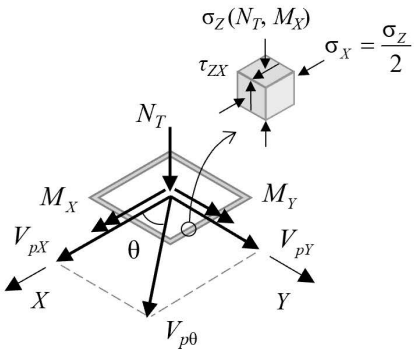
(b)


h_{inf} / h_c
1
0.8
0.6
0.4
0.2
0
h_c
h_{inf}
23
25
27
29
Time [s]
Z
Y
(a)
h_{inf} / h_c
1
0.8
0.6
0.4
0.2
0
23
25
27
29
Time [s]
Z
X
(b)

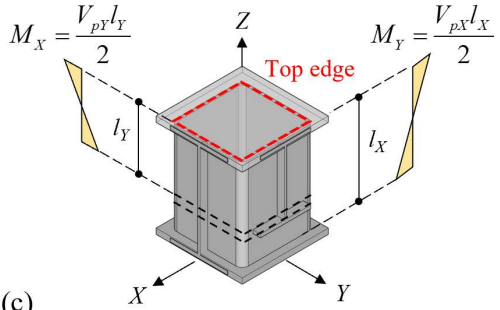

1800
900
0
-900
-1800
Shear force V_Y [kN]
K_v
V_p
$-V_p$
End
(Start)
-0.012 -0.006 0 0.006 0.012
Shear deformation γ_Y [rad]
(a)
Shear force V_X [kN]
Start
End
Shear deformation γ_X [rad]
(b)
A
B
$V_{pY,A}$
$V_{pY,B}$
(c)
$V_{pX,B}$
$V_{pX,A}$
(d)


Z
$M_X = \frac{V_{pY} l}{2}$
$M_Y = \frac{V_{pX} l}{2}$
l
l
Y-panel
X-panel
X
Y

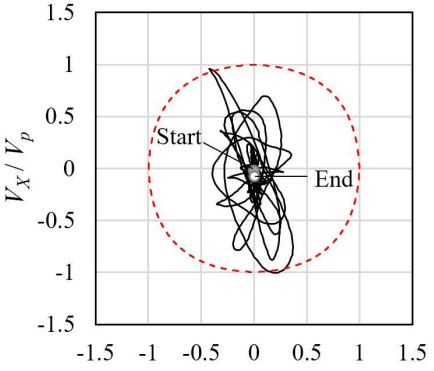
(a)


$\sigma_Z(N_T, M_X)$
$\sigma_X = \frac{\sigma_Z}{2}$
τ_{ZX}
N_T
M_X
M_Y
V_{pX}
θ
V_{pY}
X
Y
$V_{p\theta}$

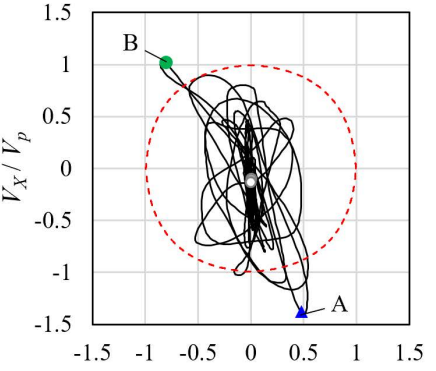
(b)


$M_X = \frac{V_{pY} l_Y}{2}$
Z
Top edge
$M_Y = \frac{V_{pX} l_X}{2}$
l_Y
l_X
X
Y

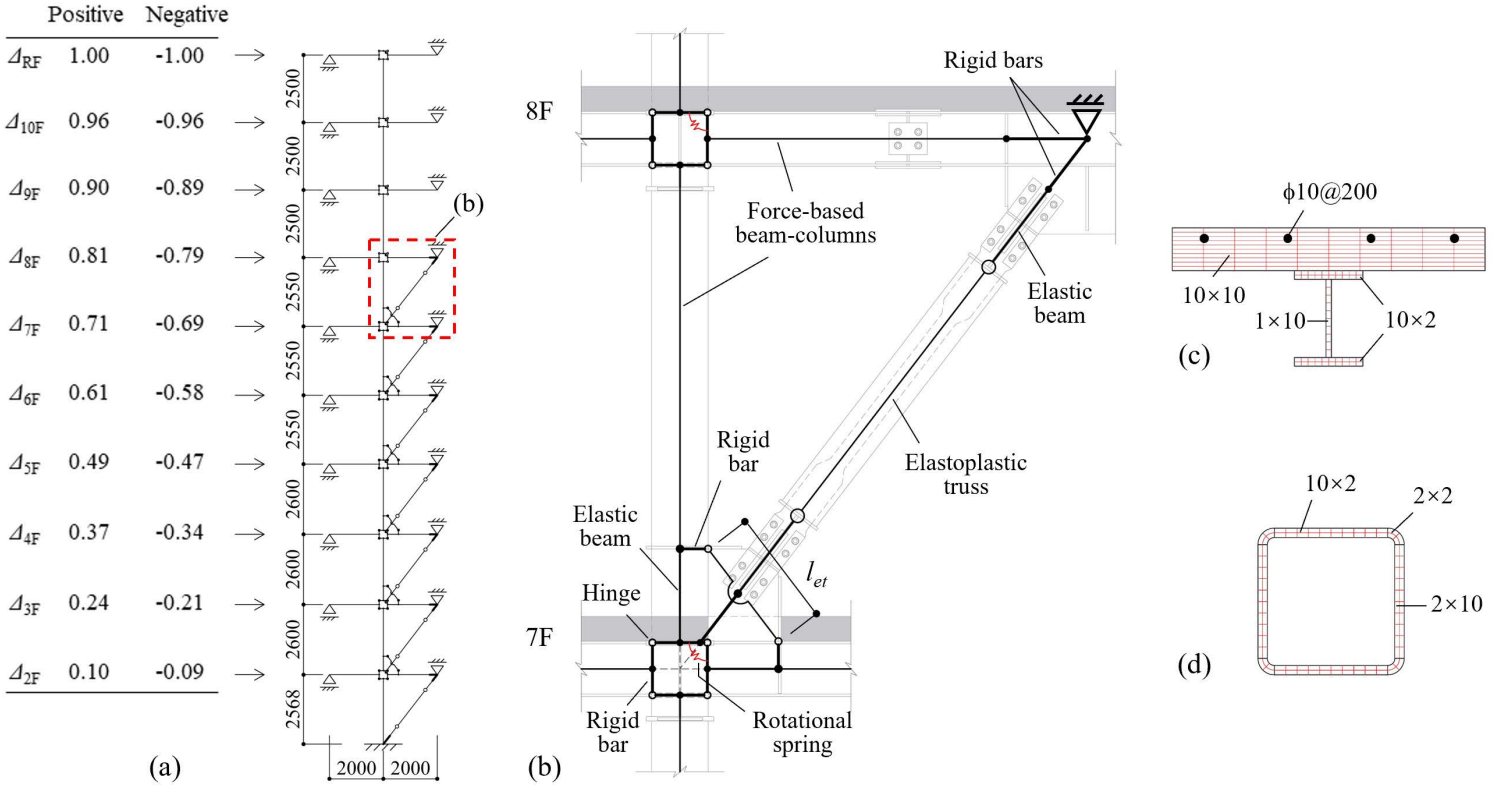
(c)

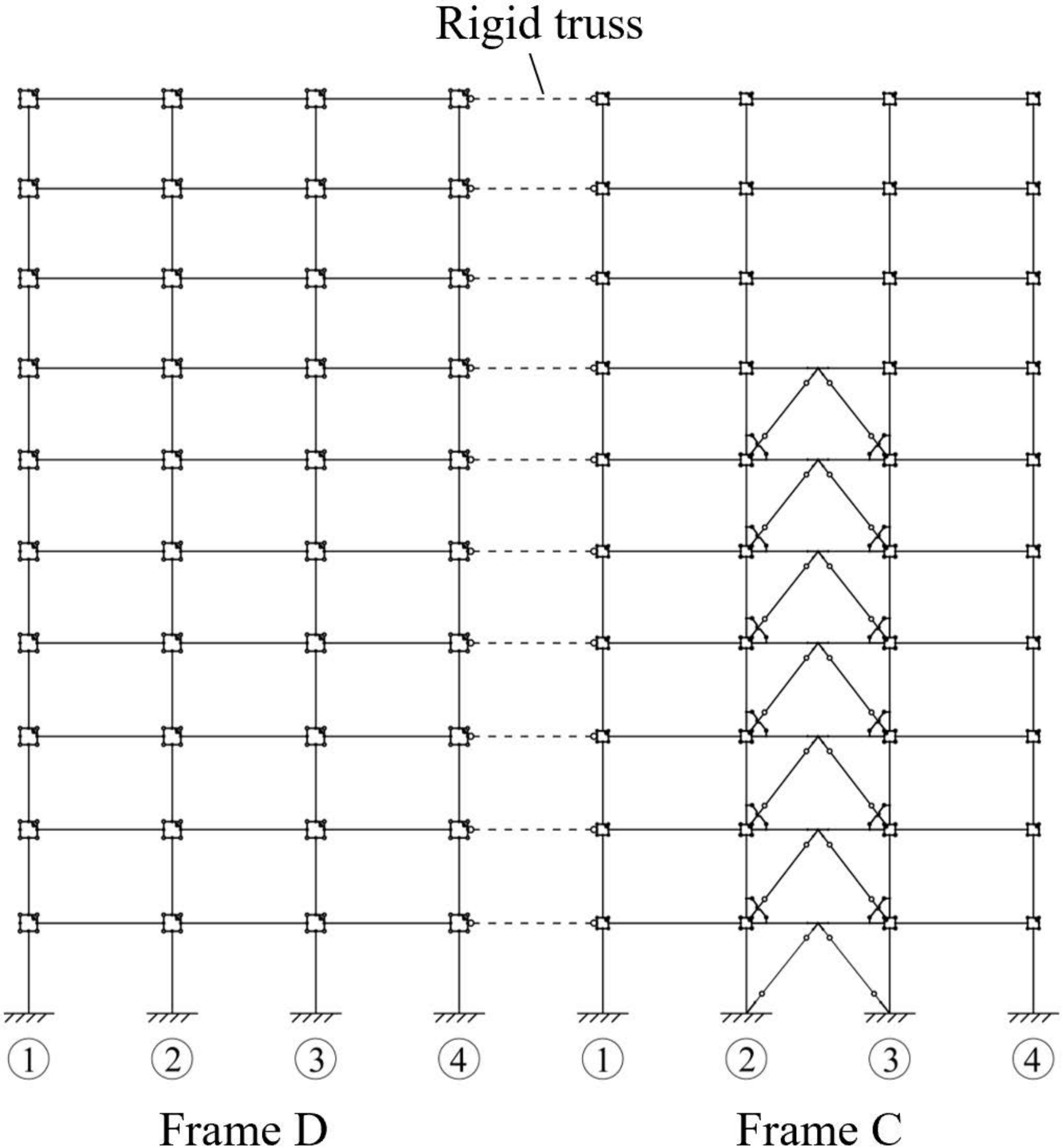

1.5
1
0.5
0
-0.5
-1
-1.5
-1.5 -1 -0.5 0 0.5 1 1.5
V_X / V_p
V_Y / V_p
Start
End

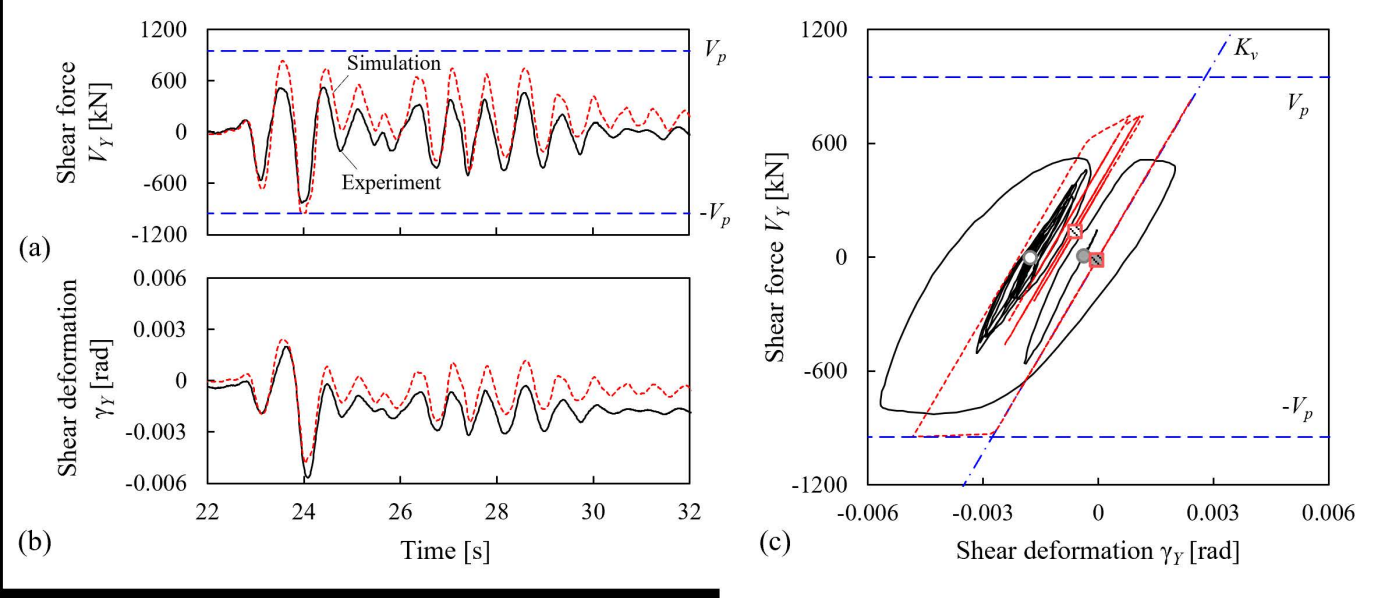
(a)


1.5
1
0.5
0
-0.5
-1
-1.5
-1.5 -1 -0.5 0 0.5 1 1.5
V_X / V_p
V_Y / V_p
B
A

(b)


Positive
Negative
Δ_RF 1.00 -1.00
Δ_10F 0.96 -0.96
Δ_9F 0.90 -0.89
Δ_8F 0.81 -0.79
Δ_7F 0.71 -0.69
Δ_6F 0.61 -0.58
Δ_5F 0.49 -0.47
Δ_4F 0.37 -0.34
Δ_3F 0.24 -0.21
Δ_2F 0.10 -0.09
2500
2500
2500
2550
2550
2550
2600
2600
2600
2568
(b)
2000 2000
(a)
8F
Rigid bars
Force-based beam-columns
Elastic beam
Elastoplastic truss
Rigid bar
Elastic beam
Hinge
l_{et}
7F
Rigid bar
Rotational spring
(b)
ϕ10@200
10×10
1×10
10×2
(c)
10×2
2×2
2×10
(d)


Rigid truss
1
2
3
4
1
2
3
4
Frame D
Frame C


1200
600
0
-600
-1200
Shear force
V_Y [kN]
Simulation
Experiment
V_p
$-V_p$
(a)
0.006
0.003
0
-0.003
-0.006
Shear deformation
γ_Y [rad]
22
24
26
28
30
32
Time [s]
(b)
K_v
V_p
$-V_p$
Shear force V_Y [kN]
-0.006
-0.003
0
0.003
0.006
Shear deformation γ_Y [rad]
(c)